

# YSO jets in the Galactic plane from UWISH2 – V. Jets and outflows in M17

M. R. Samal,<sup>1★</sup> W. P. Chen,<sup>1★</sup> M. Takami,<sup>2</sup> J. Jose<sup>3,4</sup> and D. Froebrich<sup>5</sup>

<sup>1</sup>Graduate Institute of Astronomy, National Central University 300, Zhongli City, Taoyuan County 32001, Taiwan

<sup>2</sup>Institute of Astronomy and Astrophysics, Academia Sinica, PO Box 23-141, Taipei 10617, Taiwan

<sup>3</sup>Indian Institute of Science Education and Research, Rami Reddy Nagar, Karakambadi Road, Mangalam (PO) Tirupati 517507, India

<sup>4</sup>Kavli Institute for Astronomy and Astrophysics, Peking University, Yi He Yuan Lu 5, Haidian Qu, Beijing 100871, China

<sup>5</sup>Centre for Astrophysics, and Planetary Science, The University of Kent, Canterbury, Kent CT2 7NH

Accepted 2018 March 27. Received 2018 March 27; in original form 2017 December 11

## ABSTRACT

Jets and outflows are the first signposts of stellar birth. Emission in the H<sub>2</sub> 1–0 S(1) line at 2.122- $\mu$ m is a powerful tracer of shock excitation in these objects. Here we present the analysis of  $2.0 \times 0.8 \text{ deg}^2$  data from the UK Wide-field Infrared Survey for H<sub>2</sub> (UWISH2) in the 1–0 S(1) line to identify and characterize the outflows of the M17 complex. We uncover 48 probable outflows, of which 93 per cent are new discoveries. We identified driving source candidates for 60 per cent of outflows. Among the driving source candidate young stellar objects (YSOs), 90 per cent are protostars and the remaining 10 per cent are Class II YSOs. In comparison with results from other surveys, we suggest that H<sub>2</sub> emission fades very quickly as the objects evolve from protostars to pre-main-sequence stars. We fit spectral energy distribution (SED) models to 14 candidate outflow-driving sources and conclude that the outflows of our sample are mostly driven by moderate-mass YSOs that are still actively accreting from their protoplanetary disc. We examined the spatial distribution of the outflows with the gas and dust distribution of the complex and observed that the filamentary dark cloud M17SWex, located on the south-western side of the complex, is associated with a greater number of outflows. We find that our results corroborate previous suggestions that, in the M17 complex, M17SWex is the most active site of star formation. Several of our newly identified outflow candidates are excellent targets for follow-up studies to understand better the very early phase of protostellar evolution.

**Key words:** stars: formation – ISM: HII regions – ISM: individual objects: Galactic plane – ISM: jets and outflows – infrared: stars.

## 1 INTRODUCTION

Jets and outflows are common signatures of stellar birth. They are thought to represent two aspects of the same mass-loss phenomenon responsible for removal of angular momentum from the star–disc system, allowing accretion to proceed and the star to grow. Observationally, a strong correlation between mass accretion and mass-loss has been observed in young stars (e.g. Hartmann et al. 1998), favouring the fact that outflows indeed play a significant role in the growth and evolution of young stars. In this context, while much has been learned about the evolved class II–III phases of pre-main-sequence (PMS) stars from observations and modelling (e.g. Cabrit 2007), the evolution of class 0/I objects, where the roles of outflows are

significant and stars obtain most of their mass, is less understood. Similarly, another important related question concerning outflows is the driving mechanisms. Models fall broadly into two categories: arising from the interface between the star’s magnetosphere and disc, i.e. the X-wind model, and arising from a wide range of disc radii, i.e. the disc–wind model (details can be found in Ray 2007). Understanding which one of the two models is dominant requires investigation of a large sample of outflow-bearing young stars, as outflows show a wide variety of morphologies (e.g. Arce et al. 2007, and references therein). Therefore, detecting and characterizing outflows from the youngest protostellar sources holds the key towards understanding the evolution of protostars as well as their launching mechanisms.

In this context, near-infrared emission at 2.12- $\mu$ m (H<sub>2</sub>  $\nu = 1-0$  S(1)) is one of the ideal tools to search for shock-excited outflows in terms of jets and knots from young sources. This line is an excellent tracer of hot ( $T \sim 2000$  K) and dense ( $n \geq 10^3 \text{ cm}^{-3}$ ) gas excited by

\* E-mail: manash.samal3@gmail.com (MRS); wchen@astro.ncu.edu.tw (WPC)

the fast shocks ( $10\text{--}100\text{ km s}^{-1}$ ) caused by the interactions of jets with the surrounding interstellar medium (e.g. Stanke, McCaughrean & Zinnecker 2002). Moreover, for large-scale studies, outflow morphologies with near-infrared observations are more successful in identifying outflow-driving sources (particularly in the crowded region) compared with molecular observations, which typically lack the spatial resolution and depth to identify fainter outflows. Jets are believed to be the highly compressed ejecta of accelerated entrained gas of the ambient medium. Jets and winds drive slower moving molecular lobes called bipolar molecular outflows.

Although many studies using  $\text{H}_2$  observations have focused on identification and characterization of outflow sources in nearby clouds (e.g. Hodapp 2007; Davis et al. 2007, 2009; Kumar et al. 2011; Khanzadyan et al. 2012; Bally et al. 2014; Zhang et al. 2015), searches for outflow sources on Galactic scales are still lacking. In the last decade, a few hundred individual young stellar objects (YSOs) with outflows, i.e. so-called ‘extended green objects’ (EGOs), have been identified in the Galactic plane using the *Spitzer* 4.5- $\mu\text{m}$  band observations (e.g. Cyganowski et al. 2008, 2009) of the Galactic Legacy Infrared Mid-Plane Survey Extraordinaire (GLIMPSE) survey. GLIMPSE is, however, a shallow survey – the faintest EGOs identified in the GLIMPSE survey have surface brightnesses in 4.5- $\mu\text{m}$  images  $\geq 4\text{ MJy sr}^{-1}$ . In comparison, the majority of the diffuse green emission in NGC1333 (distance  $\sim 250\text{ pc}$ ) has 4.5- $\mu\text{m}$  surface brightness  $\leq 4\text{ MJy sr}^{-1}$  (Gutermuth et al. 2008). Thus GLIMPSE survey is more sensitive to massive young stellar object (MYSO) outflows in distant star-forming regions.

Advanced wide-field sensitive infrared telescopes in recent years have enabled explorations of outflow candidates in the infrared waveband over Galactic scales. In this regard, the United Kingdom Infrared Telescope (UKIRT) Wide-field Infrared Survey for  $\text{H}_2$  (UWISH2; Froebrich et al. 2011) conducted with UKIRT at 2.12- $\mu\text{m}$  ( $\text{H}_2\ v = 1\text{--}0\text{ S}(1)$ ) has opened a new avenue to search for outflows from YSOs (e.g. Ioannidis & Froebrich 2012a,b; Froebrich & Makin 2016; Makin & Froebrich 2018), even possibly from low-mass YSOs (e.g. Ioannidis & Froebrich 2012b). We note that the surface brightness limit of the UWISH2 survey in the  $\text{H}_2$  narrow-band filter is 300–2000 times better than the  $\text{H}_2$  emission strength of the GLIMPSE survey in the 4.5- $\mu\text{m}$  band (Froebrich et al. 2011), thus in general a likely better tracer of outflows; however, we emphasize that in the region of high extinction the visibility of  $\text{H}_2$  emission can be poor compared with 4.5- $\mu\text{m}$  emission. Moreover, in the context of protostar detection, in recent years the instruments of the *Spitzer* Space Telescope and the *Herschel* Space Observatory have improved resolution and sensitivity in the mid- and far-infrared domain, where protostars emit the bulk of their energy. In fact, many well-known class 0/I protostars have been detected between 3.6 and 8- $\mu\text{m}$  with rising spectral energy distributions (SEDs) between 24 and 70- $\mu\text{m}$  (e.g. Enoch et al. 2009; Manoj et al. 2013; Dunham et al. 2015). Combining *Spitzer* and *Herschel* data with 2.12- $\mu\text{m}$  observations, therefore, it is now possible to identify deeply embedded outflow-bearing class 0/I protostars in a star-forming complex that are too faint or extincted to be detected with the previous shorter-wavelength facilities (e.g. the Two Micron All Sky Survey (2MASS), UKIRT Infrared Deep Sky Survey (UKIDSS) and GLIMPSE Survey).

In this work, we make use of UWISH2, *Spitzer* and *Herschel* data to identify and characterize the outflow-driving young protostars of the M17 cloud complex, which is at a moderate distance and currently producing young stars at a high rate. This work is organized as follows: Section 2 describes the M17 complex. Section 3 discusses

the various data sets and photometric catalogues. In Section 4, we discuss the identification of outflows and outflow-driving candidate YSOs and physical properties of candidate YSOs by fitting the YSO models to their observed SEDs. Section 5 discusses the general nature of outflows, comparison with other similar surveys and also presents a few interesting cases. Section 6 describes the star formation scenario of M17 with the aid of the spatial distribution and correlation of identified outflows with the gas and dust of the complex. Section 7 summarizes the various results obtained.

## 2 THE M17 COMPLEX

M17 ( $l \sim 15^\circ.09, b \sim -00^\circ.75$ ), located at the north-east edge of one of the largest giant molecular clouds (size  $\sim 70\text{ pc} \times 15\text{ pc}$  and mass  $\geq 2 \times 10^5\text{ M}_\odot$ ; Elmegreen, Lada & Dickinson 1979) in the Sagittarius–Carina arm of our Galaxy, is a blister  $\text{H II}$  region (also known as the Omega Nebula, W38, S45) and is the second brightest thermal radio source in the sky after Orion. It is illuminated by the massive, 1–3 Myr old (Jiang et al. 2002) stellar cluster NGC 6618, the earliest O stars of which consist of an O4–O4 binary called ‘Kleinmann’s Anonymous Star’.

The giant molecular cloud (GMC), as observed in low-resolution ( $\sim 2.3\text{ arcmin}$ )  $^{13}\text{CO}$ , contains four major fragments, namely A, B, C and D, each of mass  $\geq 4 \times 10^4\text{ M}_\odot$  (Elmegreen et al. 1979). The local standard-of-rest velocity ( $V_{\text{LSR}}$ ) and line width of these components are in the range  $20\text{--}22\text{ km s}^{-1}$  and  $3.8\text{--}5.1\text{ km s}^{-1}$ , respectively. From the velocity structure of the  $^{12}\text{CO}$  and  $^{13}\text{CO}$  gas, Elmegreen et al. (1979) suggest that most of the CO emission of the GMC comes from a single cloud of velocity around  $20\text{ km s}^{-1}$ , although the cloud has fragmented and there is a gradual change in velocity structure in the complex from north-east to south-west. The peak velocity increases from  $20 \pm 1\text{ km s}^{-1}$  in the north-east to about  $22 \pm 1\text{ km s}^{-1}$  in the extreme south-west. They argued that these differences in velocity pattern may be related to the recent passage of a spiral density wave, which would have moved from north-east to south-west in this part of the Galaxy.

Fig. 1 shows the overview of the complex, with all the above components marked. It also shows the distribution of ionized gas associated with the  $\text{H II}$  region. Among the fragments, the high-excitation temperature and compact fragments, A and B, are located on the north-east side of the complex very close to the  $\text{H II}$  region, whereas the low-excitation temperature and larger fragments, C and D, are located further away from the  $\text{H II}$  region in its south-western direction. Among the fragments, fragment B is usually referred to as M17 SW (Thronson & Lada 1983; Guesten & Fiebig 1988), while, after the discovery of a flying-dragon-like dark cloud by *Spitzer* in the extended region of M17 SW (i.e. in the D component of the GMC), the D component is usually known as M17 SWex (Povich & Whitney 2010; Povich et al. 2013). The infrared dark cloud (IRDC) G14.225–0.506 comprises the central region of M17 SWex, where dense filamentary ammonia gas (at  $V_{\text{LSR}} \sim 20\text{ km s}^{-1}$ ) and hub systems have been observed (Busquet et al. 2013). Additionally, Povich et al. (2007), from CO observations, detected a coherent shell-like structure on the eastern side of the  $\text{H II}$  region with local standard-of-rest velocity ( $V_{\text{LSR}} \sim 19\text{ km s}^{-1}$ ). The shell is coincident with the bubble walls of a cavity observed in the *Spitzer* images (Fig. 1). Povich et al. (2007) named it the M17 extended bubble (M17 EB).

The  $V_{\text{LSR}}$  and full width at half-maximum (FWHM) line width of the ionized gas associated with the  $\text{H II}$  region are  $18.6$  and  $3.2\text{ km s}^{-1}$ , respectively (Joncas & Roy 1986). Since the velocities of the various dense components (Elmegreen et al. 1979; Busquet et al.

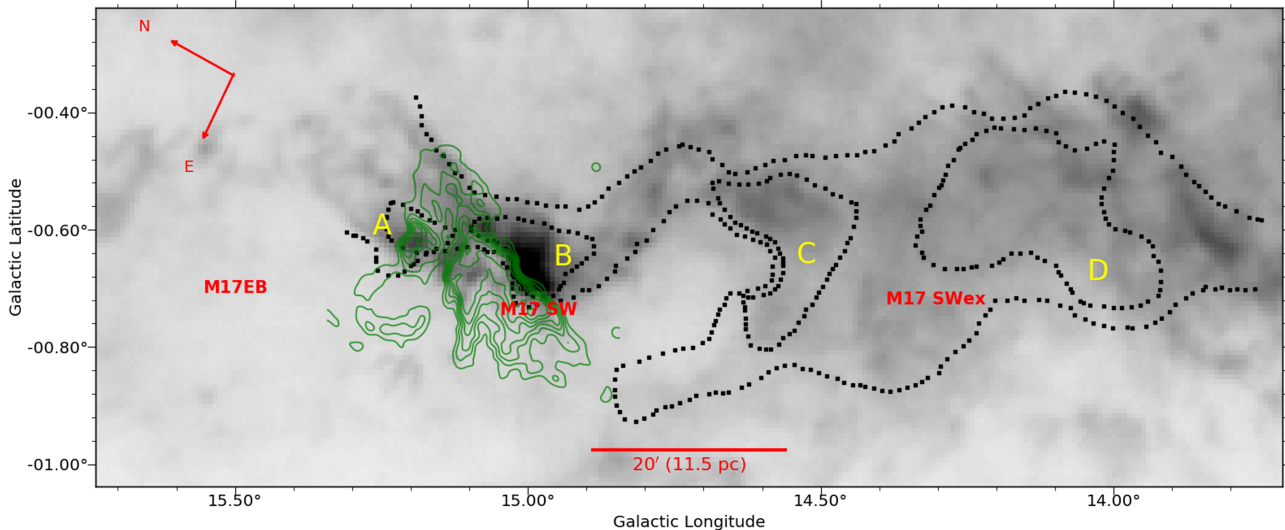


**Figure 1.**  $^{12}\text{CO}$  map (grey-scale) of the M17 complex showing the distribution of molecular gas. The map is obtained at a resolution of  $\sim 46$  arcsec with the Purple Mountain Observatory (PMO) 13.7-m telescope (Jiang et al., in preparation). The green contours correspond to the VLA 20 cm (at 0.05, 0.14, 0.24, 0.34, 0.43, 0.53, 0.63, 0.73, 0.83 and 0.93  $\text{Jy beam}^{-1}$ ; resolution  $\sim 6$  arcsec) emission from Helfand et al. (2006), while the black contours represent the  $^{13}\text{CO}$  emission (at 5 and 10 K; resolution  $\sim 2.3$  arcmin) from Elmegreen et al. (1979). The field size is  $\sim 2.0 \times 0.8 \text{ deg}^2$  (or  $70 \times 28 \text{ pc}^2$ ). The four dense fragments, which have been designated by the letters A (in the north-east) to D (in the extreme south-west) are also marked.

2013) are similar to the ionized gas velocity of M17, the bright  $\text{H II}$  region and the dense fragments are part of the same cloud. The spectrophotometric distance for NGC 6618 is estimated to be in the range 2.1–2.2 kpc (Chini, Elsaesser & Neckel 1980; Hoffmeister et al. 2008), consistent with the kinematic distance  $\sim 2.2$  kpc obtained from radial velocity measurements of the ionized gas (Georgelin, Georgelin & Roux 1973; Joncas & Roy 1986). Along the same line, using the trigonometric parallax of  $\text{CH}_3\text{OH}$  masers ( $V_{\text{LSR}} \sim 23 \pm 3 \text{ kms}^{-1}$ ), recent very-long-baseline interferometry (VLBI) observations have estimated a distance of  $1.98^{+0.14}_{-0.12}$  kpc (Wu et al. 2014) to M17, which we have adopted in this work.

Star formation towards M17 has been extensively studied by Povich et al. (2007), Povich & Whitney (2010) and Povich et al. (2016). Their results suggest that M17 is currently producing stars at a rate  $\geq 0.005 M_{\odot} \text{ yr}^{-1}$ , about four times the star formation rate of the Orion Nebula Cluster (see Povich et al. 2016). Thus a potential site at which one would expect a large number of protostars. In the present work, we focus our study on an area  $\sim 2.0 \times 0.8 \text{ deg}^2$  of the complex, primarily covering the dense clouds and the extended bubble.

### 3 OBSERVATIONS AND DATA SETS

We retrieved narrow-band continuum-subtracted  $\text{H}_2 \nu = 1-0 \text{ S}(1)$  2.12- $\mu\text{m}$  images from the UWISH2 data base<sup>1</sup> (Froebrich et al. 2011). UWISH2 is an unbiased survey of the inner Galactic plane in the  $\text{H}_2$  line at 2.12- $\mu\text{m}$ , using the Wide-Field Camera (WFCAM) camera at UKIRT. The survey covers  $\sim 209 \text{ deg}^2$  along the inner Galactic plane from  $l \approx 357^\circ$  to  $l \approx 65^\circ$  and  $|b| \leq 1^\circ.5$ . WFCAM houses four Rockwell Hawaii-II (HgCdTe 2048  $\times$  2048) arrays spaced by 94 per cent in the focal plane. For UWISH2 observations, 12 exposures were acquired at each telescope pointing, resulting in a total exposure time per pixel of 720 s. The typical FWHM of the stellar point-spread function (PSF) of the UWISH2 observations is

0.7 arcsec, the typical  $5\sigma$  detection limit of point sources is  $\sim 18$  mag and the surface brightness limit is  $\sim 4.1 \times 10^{-19} \text{ W m}^{-2}$ . In order to perform continuum subtraction of narrow-band images, UWISH2 uses UKIDSS data in the  $K$  band (2.2- $\mu\text{m}$ ) taken with the same telescope and instrumental set-up as part of the Galactic Plane Survey (GPS; Lucas et al. 2008). The GPS survey maps 1800  $\text{deg}^2$  of the Galactic plane ( $|b| < 5^\circ$ ) in the  $J$ ,  $H$  and  $K$  bandpasses with total exposure time per pixel of 80, 80 and 40 s, respectively, reaching  $5\sigma$  detection limits of  $J \sim 19.8$ ,  $H \sim 19.0$  and  $K \sim 18.0$  mag, respectively. The typical FWHM of the GPS survey is 0.9 arcsec. We used the continuum-subtracted  $\text{H}_2$  images to identify jets and knots in the M17 complex.

The M17 complex was observed by the *Spitzer* Space Telescope as part of the GLIMPSE survey (Benjamin et al. 2003) and the Multiband Imaging Photometer GALactic plane survey (MIPSGAL; Carey et al. 2009). We obtained Post Basic Calibrated Data (PBCD) images of the *Spitzer* Infrared Array Camera (IRAC) at 3.6, 4.5, 5.8 and 8.0- $\mu\text{m}$  and of the Multiband Imaging Photometer (MIPS) at 24.0- $\mu\text{m}$  from the *Spitzer* Archive<sup>2</sup> to search for embedded YSOs and to examine the morphology of the interstellar medium (ISM) at the location of jets and knots. For point sources, we used the UKIDSS  $JHK$  (Lucas et al. 2008), GLIMPSE IRAC (Carey et al. 2009) and MIPSGAL 24- $\mu\text{m}$  (Gutermuth & Heyer 2015) point-source catalogues available on the VizieR<sup>3</sup> interface. Note that the 3.6- and 4.5- $\mu\text{m}$  bands are more sensitive to stellar photospheres than the 5.8, 8.0 and 24- $\mu\text{m}$  bands and the angular resolution of the images in the IRAC bands is in the range 1.7–2.0 arcsec, whereas in the MIPS 24- $\mu\text{m}$  band it is  $\sim 6.0$  arcsec.

For this work, we also downloaded 70- $\mu\text{m}$  images from the *Herschel* Science Archive,<sup>4</sup> observed as part of the Hi-GAL survey (Molinari et al. 2010), using the Photodetector Array Camera and Spectrometer (PACS). The angular resolution of the Hi-GAL data

<sup>2</sup><http://sha.ipac.caltech.edu/applications/Spitzer/SHA/>

<sup>3</sup><http://vizier.u-strasbg.fr/viz-bin/VizieR-4>

<sup>4</sup><http://archives.esac.esa.int/hsa/whsa/>

<sup>1</sup><http://astro.kent.ac.uk/uwish2/>

at 70- $\mu\text{m}$  is  $\sim 10$  arcsec. To obtain point-source fluxes, we performed photometry on the *Herschel* 70- $\mu\text{m}$  image using the IRAF tasks *daofind* and *apphot* to extract the positions of the sources and to perform aperture photometry. We used an aperture radius of 12 arcsec and inner and outer sky annuli of 35 and 45 arcsec, respectively and applied the aperture correction as documented by the PACS team (Balog et al. 2014). Since our target sources are embedded in strongly varied spatial structures, the variations in the background limit the photometric accuracy. We thus used different apertures and estimated that our photometry is accurate within 10–15 per cent.

The above point-source catalogues are used to identify the YSOs in the vicinity of the jets/knots and construct their SEDs. Note that the MIPS GAL 24- $\mu\text{m}$  catalogue comes along with its GLIMPSE-IRAC counterparts. For making various colour–colour or colour–magnitude plots between 3.6 and 70- $\mu\text{m}$  (in the search for YSOs close to the knots and jets), we matched the astrometric position of the MIPS GAL 24- $\mu\text{m}$  catalogue with the astrometric position of the 70- $\mu\text{m}$  sources using a position-matching tolerance of 6 arcsec<sup>5</sup> (the FWHM of the 24- $\mu\text{m}$  data). To obtain the SEDs of the selected YSOs, we inspected the images and catalogues of the YSOs visually using the ALADIN software, then matched the already made 3.6–70- $\mu\text{m}$  catalogue to the UKDISS catalogue using a matching radius of 2 arcsec (the FWHM of the GLIMPSE data) to obtain data points between 1.2 and 70- $\mu\text{m}$ . In a few cases, where there was more than one source within the matching radius, we considered the closest one as the best match.

In addition, we also exploit information from the following major available surveys in search for early stages of star formation, such as cold cores/clumps or SiO emission, in the vicinity of the jets/knots.

(i) We used the Csengeri et al. (2014) catalogue of compact objects from the APEX Telescope Large Area Survey of the Galaxy (ATLASGAL) at 870- $\mu\text{m}$  (beam  $\sim 19.2$  arcsec, sensitivity  $\sim 50$ – $70$  mJy beam<sup>-1</sup>) for identifying clumps/cores.

(ii) We used the Rosolowsky et al. (2010) catalogue of compact objects from the Bolocam Galactic Plane Survey (BGPS; Aguirre et al. 2011) at 1.1 mm (beam  $\sim 33$  arcsec, sensitivity  $\sim 30$ – $60$  mJy beam<sup>-1</sup>) for identifying clumps/cores.

(iii) Reid & Wilson (2006) used the Submillimeter Common-User Bolometer Array (SCUBA) on the James Clerk Maxwell Telescope (beam  $\sim 15.4$  arcsec, sensitivity  $\sim 27$  mJy beam<sup>-1</sup>) to map an approximately 12 arcmin  $\times$  12 arcmin region around the M17 H II region at 850- $\mu\text{m}$ . We used their catalogue for our analysis.

(iv) SiO emission is a strong signpost of outflows from the very youngest, class 0/I, sources (e.g. Gibb et al. 2004; Codella et al. 2007; Tafalla et al. 2015), although other explanations are possible, such as low-velocity shocks caused by large-scale flow collisions during global collapse or the dynamical interaction of two clouds (e.g. see López-Sepulcre et al. 2016, and references therein). Recently, Csengeri et al. (2016) conducted a survey on massive clumps with the IRAM 30-m and APEX telescopes at the frequency of the SiO (2–1) and (5–4) transitions. In the present work, we used the catalogue of Csengeri et al. (2016) in search of SiO emission at the location of the MHOs, although this sample is only for clumps of mass greater than  $650 M_{\odot}$ . Note that the spatial position of the shock-excited SiO and 2.12- $\mu\text{m}$  emission for a given outflow can be different, as they are sensitive to different physical conditions.

We note, owing to the different resolutions of the above mm–submm surveys, that when we have multiple spatial positions for a given clump we considered the spatial position of the highest resolution as the better representation of its true position. We also note that the association of individual clumps/cores of the above surveys with the M17 complex required velocity information. However, it is worth mentioning that there are mainly two cloud components in the direction of M17 (particularly in the direction of C and D components), at  $V_{\text{LSR}} \sim 20$  and 40 (Lada 1976); as seen by <sup>13</sup>CO, emission from the latter component is distributed mainly in the latitude range  $-0.2^{\circ}$  to  $0.00^{\circ}$  (e.g. Umemoto et al. 2017), therefore unrelated to the area studied in this work. Moreover, from the work of Busquet et al. (2013) one can find that the most dense dust continuum clumps of M17SWex coincide positionally with the velocity of the ammonia gas at  $V_{\text{LSR}} \sim 20 \pm 2$  km s<sup>-1</sup>. Since dense gas is more related to star formation, we thus assume that contamination of other line-of-sight Galactic dust clumps should be less in our studied area.

## 4 RESULTS

### 4.1 Identification of outflows and outflow-driving sources

Our first goal is to identify shocked H<sub>2</sub> features. To do so, we searched for jets or knots or bow-shock features in continuum-subtracted (H<sub>2</sub> –K) images. These sources tend to show up as enhanced emission over the background H<sub>2</sub> –K image. However, identifying the true shock-excited features in the H<sub>2</sub> –K images is not straightforward, as they can be confused with several other artefacts. These include, but are not limited to, the following: (i) fluorescence-excited features caused by the UV field from a nearby massive star; (ii) artefacts present in the residual images due to improper continuum subtraction; (iii) artefacts due to sources of high proper motion or with excess emission.

One potential way to avoid such artefacts is to look at the multiwavelength data corresponding to the H<sub>2</sub> features. We therefore checked the morphology and strength of the emission in 1.2-, 2.2-, 4.5- and 8- $\mu\text{m}$  images corresponding to each H<sub>2</sub> emission. Artefacts due to improper continuum subtraction or proper motion or artefacts of bright stars can be identified using 2.2- $\mu\text{m}$  images (e.g. see the discussion in Ioannidis & Froebrich 2012a). Similarly, fluorescence-excited H<sub>2</sub> features can be picked up using near-infrared colour-composite images and/or *Spitzer* 8- $\mu\text{m}$  images, because fluorescence-excited features appear brownish in *JKH<sub>2</sub>* RGB images, as the *J*- and *K*-band continuum filters contain additional excited emission lines (e.g. Makin & Froebrich 2018). Similarly, the 8- $\mu\text{m}$  IRAC band contains the 7.7- and 8.8- $\mu\text{m}$  emission features commonly attributed to polycyclic aromatic hydrocarbon (PAH) molecules (Reach et al. 2006), which can be excited in the photodissociation regions (PDRs) of a cloud by the absorption of UV photons from nearby massive stars (e.g. Povich et al. 2007). Thus, the close resemblance of diffuse H<sub>2</sub> and 8- $\mu\text{m}$  emission at the peripheries of H II regions or structures pointing towards massive stars is more likely a representation of UV fluorescence excitation. In contrast to 8- $\mu\text{m}$ , the 4.5- $\mu\text{m}$  band contains both H<sub>2</sub> and CO lines, which can become bright in the presence of shocked molecular gas, such as that expected from protostellar outflows (e.g. see the discussion in Noriega-Crespo et al. 2004; Takami et al. 2010, 2011). Hence, enhanced diffuse emission at 4.5- $\mu\text{m}$  at the location of H<sub>2</sub> emission features is a supportive indication of the presence of a shocked outflow, although part of the 4.5- $\mu\text{m}$  emission could be scattered continuum light from the embedded YSOs (Takami et al. 2012). In the literature, outflows identified based on enhanced

<sup>5</sup>We note the astrometric accuracy of the MIPS GAL images is better than 1 arcsec, while it is less than 2 arcsec for the Hi-Gal images.

extended 4.5- $\mu\text{m}$  emission are referred to as ‘EGOs’ (e.g. Cyganowski et al. 2008) or ‘Green Fuzzies’ (e.g. De Buizer & Vacca 2010) and are generally identified by making IRAC colour-composite images (using 8.0-, 4.5- and 3.6- $\mu\text{m}$  bands as red, green and blue colours, respectively), as the 4.5- $\mu\text{m}$  emission stands out against other IRAC-band emission. In this work, we have also used the *Spitzer* 4.5- and 8.0- $\mu\text{m}$  bands as a tool by making IRAC colour-composite images to search for extra outflow components (if any) in the vicinity of 2.12- $\mu\text{m}$  features (particularly in highly extinguished regions of a cloud, such as dense clumps, as the extinction effect in the 4.5- $\mu\text{m}$  band is nearly half of that of the *K* band) or to trace the PDRs around massive stars.

We also looked at the morphology of the  $\text{H}_2$  features to disentangle possible planetary nebulae (e.g. see the discussion in Ramos-Larios et al. 2017) from wide-angle outflows.

Admittedly, the above criteria for identifying  $\text{H}_2$  features are somewhat subjective and the possibility of missing faint and small  $\text{H}_2$  emission features exists. None the less, comparing the number of shocked  $\text{H}_2$  features identified by us with the automatically generated shocked  $\text{H}_2$  catalogue of the UWISH2 survey (Froeblich et al. 2015), we find that both catalogues are in good agreement with each other. For example, both the catalogues have 93 per cent common sources. This ensures that the identified  $\text{H}_2$  features are highly reliable and affirms that the false-positive rate in the UWISH2 catalogue, if present at all, is likely to be less than 7 per cent.

The acronym ‘MHO’ stands for molecular hydrogen emission-line object associated with jets and outflows (Davis et al. 2010). Several clusters of  $\text{H}_2$  shock features in the region can be clearly associated with coherent outflows. We therefore followed the procedure outlined in Davis et al. (2010), i.e., when it is possible to correlate multiple knots or jets with a single outflow, we assigned them as a single MHO; otherwise, we considered each discrete jet or knot as an MHO. Briefly, we inspected large-scale  $\text{H}_2$  images in the search for possible large-scale flows. On the large-scale images, we looked for possible bow-shock features or aligned jets/knots. We then extended a line tracing the middle of the bow-shocks or knot/jets in search for possible counter bow-shocks or jets/knots in the opposite symmetric axis. For only a few cases, we observed a chain of jets/knots over parsec-scale dimensions, but the majority of the jets/knots are found to be isolated or confined to only small spatial scales. We then, based on the appearance/shape of the emission features and the alignment of features with each other and/or the potential driving sources, assigned an MHO number to a jet/knot or a chain of jets/knots or a group of jets/knots (explained in more detail below). With the above approach, we identified 48 likely outflows within our surveyed area. We list their positions in Table 1, while their distribution in the complex and correlation with cold gas at 870- $\mu\text{m}$  and shocked SiO emission are shown in Fig. 2. We discuss the general star formation of the complex with the aid of these distributions in Section 6. We note, as grouping weak emission features into an outflow is a complex problem, thus in this work we treat each identified outflow (particularly those without a driving source) as a candidate, pending verification through other shock tracers (e.g. Plunkett et al. 2013; Zinchenko et al. 2015), though most of them will very likely turn into true outflows.

Here we describe our methodology of identifying YSOs and cores and connecting them to jets/knots. The details concerning the classification of potential point sources into various YSO classes are given in Appendix A. In summary, keeping in mind that the visibility of a point source at any given band is a strong function of the evolutionary status of the source itself, the extinction around its vicinity and the sensitivity of that particular band, we used several

flux ratios between 3.6 and 70- $\mu\text{m}$  to classify all those potential sources that are in the close vicinity of jets/knots into different YSO classes (for details see Appendix A). When possible, we also used the available YSO catalogues from the literature. After identifying YSOs in the vicinity of jets/knots, we noticed that several jets/knots are not associated with any YSO candidates, which led us to think that these jets/knots possibly originate from molecular cores in their earliest evolutionary phases, such as the first hydrostatic cores (e.g. Pezzuto et al. 2012; Gerin et al. 2015) or 70- $\mu\text{m}$  dark cores (e.g. Feng et al. 2016; Aso et al. 2017). It is also quite possible that (i) these jets/knots are part of large flows from distant sources and (ii) the driving sources are still embedded in dense cores and are too faint to be detected in the *Spitzer* and *Herschel* bands (see Section 5.1 for further discussion). To account for those sources that are either in the earliest evolutionary phases or deeply embedded in dense cores, we searched for the early stages of star formation, such as cold cores/clumps or infrared dark cloud fragments or SiO emission (see Section 3), in the vicinity of the jets/knots. After identifying YSOs and cores, in the next step we tried to connect them with the nearby jets/knots. Briefly, the outflow symmetries can be of different types – for example, as described in Bally (2007), S- and Z-shaped symmetries can occur if the outflow axis changes over time due to precession induced by a companion or interactions with sibling stars in a cluster, while a C-shaped bend of the outflow axis can occur due to motion of the surrounding gas or motion of the outflow source itself – so identifying potential outflow-driving sources is not trivial in cases of misaligned outflows. Therefore, while connecting YSOs/cores with the jets/knots, we considered all those sources with positions compatible with the various jet shapes, such as straight, curved or S-shaped. Along with the evolutionary status of the YSOs, we also used indicators such as extended 4.5- $\mu\text{m}$  and/or shock tracer SiO emission to approve or reject whether any given source or core is responsible for the jets/knots observed in its vicinity. In a few rare cases, where we have two close-by sources, we gave higher priority to the younger and luminous YSO, as luminous YSOs drive stronger outflows (e.g. Caratti o Garatti et al. 2015; Manoj et al. 2016).

Here we describe two complicated examples of our approach to the connection of potential driving sources (cores or YSOs) with jets/knots. Fig. 3 illustrates an example of our approach to the search for potential driving sources around jets/knots. As can be seen, this region consists of two elongated  $\text{H}_2$  jets. Together they appear to form an east–west flow. Three potential sources, visible in different bands between 3.6 and 70- $\mu\text{m}$  (marked as 21a, 21b and 21c in the figure), lie in the vicinity of the jets. Among the sources, source 21a lies at the centre of jets and is visible in all IRAC bands, source 21b lies at one end of the MHO and is visible only in the 70- $\mu\text{m}$  band, while source 21c lies slightly away from the flow axis and is visible only at 4.5 and 24- $\mu\text{m}$ . Any of them could be the outflow-driving source, although the possibility of 21c is less as it is not along the flow axis. The evolutionary status of sources 21a and 21b, respectively, is identified in Figs A2 and A1(c) of Appendix A. In short, source 21a is not a YSO, as its location coincides with the zone of field stars in the [5.8] versus [5.8] – [8.0] diagram, it has no emission at 24/70- $\mu\text{m}$  and in the literature it is not an infrared-excess YSO (e.g. Povich & Whitney 2010). On the other hand, source 21b has the characteristics of an early class 0 source and it is bright at 70- $\mu\text{m}$ . The location of 21b is somewhat intriguing, but it could be due to projection effects or anisotropy of the medium. It is worth mentioning that Froeblich & Makin (2016), in their study of the Cassiopeia and Auriga complex, found that  $\sim 20$  per cent of bipolar flows are asymmetric in nature with length ratio  $< 0.5$ . Since there

**Table 1.** Properties of the MHOs.

ID	MHO number <sup>1</sup>	Lon. <sup>2</sup> (degree)	Lat. <sup>2</sup> (degree)	Length <sup>3</sup> (pc)	Source Type. <sup>4</sup>	Luminosity <sup>5</sup> ( $L_{\odot}$ )	Comments
01	MHO 2308	13.78040	-0.57323	0.22	class O/I	27	bipolar, two opposite symmetric streamers
02	MHO 2309	13.86546	-0.54239	–	–	–	three interconnected compact knots
03	MHO 2310	13.90317	-0.51448	–	cluster	–	group of compact knots
04	MHO 2311	13.93151	-0.49345	–	–	–	an isolated bright compact knot
05	MHO 2312	13.96643	-0.44227	–	–	–	two compact knots
06	MHO 2313	14.07504	-0.56333	0.20	class O/I	27	monopolar, elongated patchy emission
07	MHO 2314	14.08924	-0.63322	–	–	–	an isolated compact knot with some diffuse nebulosity
08	MHO 2315	14.09521	-0.63386	–	–	–	an elongated knotty structure
09	MHO 2316	14.11298	-0.57489	–	cluster	–	a patch of diffuse emission
10	MHO 2317	14.13259	-0.52206	0.45	class O/I	252	bipolar, a jet-shaped structure and two compact knots
11	MHO 2318	14.14622	-0.53602	–	–	–	an isolated compact knot
12	MHO 2319	14.17600	-0.67032	–	–	–	two aligned knot-like structures
13	MHO 2320	14.17929	-0.56165	–	class II	–	monopolar, a patch of elongated faint emission
14	MHO 2321	14.19136	-0.50404	–	cluster	13	bipolar, chain of compact knots
15	MHO 2322	14.19463	-0.52274	0.22	class I/O	53	monopolar, two compact knots
16	MHO 2323	14.20004	-0.57689	–	–	–	two faint interconnected knots
17	MHO 2324	14.21574	-0.51510	0.82	class O/I	–	bipolar, three compact jet-like structures along a line
18	MHO 2325	14.21841	-0.45140	–	–	–	a bright head–tail like structure
19	MHO 2326	14.22462	-0.66556	0.09	class O/I	34	monopolar, an elongated head–tail like structure
20	MHO 2327	14.22495	-0.57625	–	–	–	three bright knots connected with some diffuse emission
21	MHO 2328	14.24515	-0.58420	0.30	class O/I	22*	bipolar, two opposite asymmetric jets
22	MHO 2329	14.24661	-0.50227	0.30	class O/I	53*	monopolar, a jet-like structure
23	MHO 2330	14.27437	-0.53161	–	–	–	two compact knots
24	MHO 2331	14.27447	-0.57511	0.78	class O/I	19*	bipolar, chain of elongated faint emission
25	MHO 2332	14.28056	-0.49345	–	–	–	a bright compact knot
26	MHO 2333	14.31092	-0.59261	0.73	class II	286	bipolar, chain of knots, bend morphology
27	MHO 2334	14.31447	-0.53895	–	–	–	chain of elongated faint emission
28	MHO 2335	14.32700	-0.53257	0.55	core	–	monopolar, elongated faint emission
29	MHO 2336	14.33115	-0.75052	–	–	–	two bow-shock-shaped structures
30	MHO 2306	14.33145	-0.64355	0.45	class O/I	4827*	bipolar, two bright elongated knots
31	MHO 2337	14.35227	-0.58742	0.07	class O/I	4*	bipolar, two opposite symmetric jets
32	MHO 2338	14.36143	-0.63861	0.41	core	–	monopolar, a compact knot with a faint streamer
33	MHO 2339	14.36161	-0.48936	–	–	–	a bright knot with some patchy emission
34	MHO 2340	14.38114	-0.68939	–	–	–	elongated faint diffuse emission
35	MHO 2341	14.44860	-0.56711	0.38	core	–	bipolar, two opposite streamer-like structures
36	MHO 2342	14.60962	-0.52421	–	–	–	a faint elongated head–tail like structure
37	MHO 2343	14.61739	-0.60949	0.28	class O/I	–	bipolar, compact knots with some patchy emission
38	MHO 2344	14.63169	-0.57720	0.43	class O/I	715	monopolar, multiple elongated knots
39	MHO 2345	14.77681	-0.48768	0.56	class O/I	147	bipolar, chain of patchy knots along a line
40	MHO 2346	14.77861	-0.33277	0.19	class O/I	827	monopolar, an elongated continuous flow
41	MHO 2307	14.85161	-0.99178	0.19	class O/I	92	bipolar, compact bright knots
42	MHO 2347	14.85168	-0.98854	1.2	class O/I	70	bipolar, chain of knots
43	MHO 2348	14.98216	-0.67674	0.68	cluster	–	monopolar, a bow-shaped structure with a faint tail
44	MHO 2349	15.01505	-0.63124	–	–	–	a compact bright knot with a diffuse tail
45	MHO 2350	15.06827	-0.61351	0.21	core	–	bipolar, two faint lobe-like structures
46	MHO 2351	15.12872	-0.49566	0.19	class O/I	20	bipolar, three compact knots
47	MHO 2352	15.14967	-0.61683	0.24	core	–	bipolar, two opposite bright lobes
48	MHO 2353	15.25981	-0.61653	0.6	core	–	monopolar, two faint knots near to a core

<sup>1</sup> The MHO numbers are assigned in the order of their right ascensions. Prior to this work, the MHOs 2306 and 2307 have been identified by Lee et al. (2012) and Caratti o Garatti et al. (2015), respectively. Thus they appear in the middle of the table according to their right ascensions.

<sup>2</sup> The coordinates are: (i) coordinates of the driving source if one is found; (ii) coordinates of the peak intensity if the MHO constitutes an isolated knot; (iii) central coordinates of the knots if the MHO constitutes multiple knots without a driving source candidate.

<sup>3</sup> For objects with a driving source only, we measured the apparent length. Quoted lengths are end-to-end for bipolar outflows or twice the source-to-end for monopolar flows.

<sup>4</sup> We note that evolution of massive protostars differs significantly from evolution of low-mass protostars (e.g. Hosokawa & Omukai 2009); however, unlike the case of low-mass stars, there is no observational evolutionary sequence that is firmly established for high-mass stars, thus in this work we have tentatively adopted the classification of the low-mass stars for the high-mass stars.

<sup>5</sup> Luminosities are either from SED models or using only 70- $\mu$ m flux. Estimates based on the latter method are marked with asterisks. These luminosities are accurate within a factor of two.

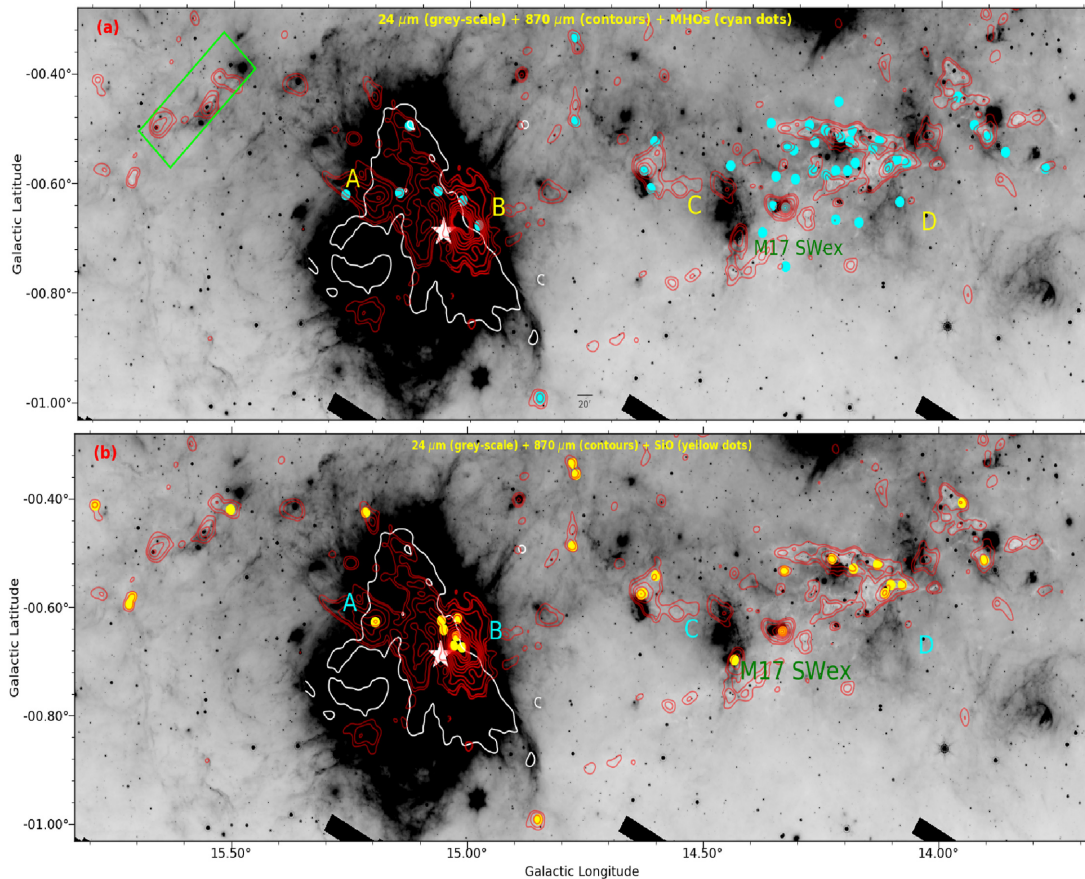


**Figure 2.** The distributions of MHO-based outflows (top panel) and SiO emission (bottom panel) in the M17 complex on the 24- $\mu\text{m}$  background image. Red contours represent 870- $\mu\text{m}$  dust continuum emission from the ATLASGAL survey. Contour levels are at geometric progression in square root two, starting at  $0.1 \text{ Jy beam}^{-1}$  and ending at  $7.5 \text{ Jy beam}^{-1}$ . The outer extent of the main H II region is shown by a white contour ( $\sim 0.05 \text{ Jy beam}^{-1}$  at 21 cm). The star symbol denotes the central location of the cluster NGC 6618. The green rectangle represents the area of the complex that is not covered by UWISH2; it lies at the edges of UWISH2 tiles.

are no other potential sources along the presumed flow axis of the jets (marked with an ellipse), 21b is therefore very likely the driving source of the jets. Fig. 4 depicts another example, where three H<sub>2</sub> jet-like features along with all the aforementioned signposts of star formation, including an EGO, have been found. As can be seen, the jet-like features lie on the eastern outskirts of an ATLASGAL clump (shown in contours) and a bright 24- $\mu\text{m}$  source (marked as ID 38) lies at the centre of the clump. One can see that the middle jet connects well with the point source through enhanced diffuse 4.5- $\mu\text{m}$  emission. The clump is also at the location of SiO emission. The column density in the direction of the clump is of the order of  $\sim 10^{23} \text{ cm}^{-2}$  (e.g. Csengeri et al. 2016), perhaps the possible reason why we do not see H<sub>2</sub> emission in the vicinity of the source. Deep high-resolution molecular observations would be needed to track the origin of these infrared jet-like structures (e.g. Plunkett et al. 2013; Zinchenko et al. 2018). None the less, it is worth mentioning that multiple wide-angle H<sub>2</sub> bullets and jet-like structures have been reported for a few cases (e.g. Sahai et al. 2008; Bally et al. 2011). The nature of such explosive outflows is still not well understood, but it is believed that it might be related to dynamical decay of a non-hierarchical system of stars or protostellar merger or close passage of two protostars (e.g. see the discussion in Bally et al. 2015, 2017; Sahai et al. 2017). In the present work, we tentatively consider that all three jet-like features are part of a single outflow and are likely driven by the point source(s) embedded in the clump.

Source 38, being luminous and class-0 type, could be the dominant source responsible for the flow.

Figs 3 and 4 are illustrations for two outflows. We followed a similar prescription for all MHOs. The detailed discussion on the individual MHOs is given in Appendix B, where we present multiwavelength large-scale ( $\sim 1 \times 1 \text{ pc}^2$  area) images around the MHOs, provide notes on individual objects and discuss their driving sources. Briefly, following the above approach, we associate 26 YSOs/cores and 4 clusters (i.e. the driving source is situated in a group of stars and we could not single it out) with the 48 MHO features. The spectral nature of the driving sources is also tabulated in Table 1. Out of 26 YSOs/cores, 6 are cores without point sources up to 70- $\mu\text{m}$ , 18 are protostars (class 0/I YSOs) and 2 are evolved sources (class II YSOs).

## 4.2 Physical properties of the driving sources

### 4.2.1 SED modelling of YSOs

To get deep insight into the nature of the YSOs identified in the present work, we modelled the observed SEDs using the models of Robitaille et al. (2006, 2007). The models used the Monte Carlo based radiation transfer code of Whitney et al. (2003a,b) to follow photons emitted by the central star as they are scattered, absorbed and re-emitted throughout the disc and envelope system. The code

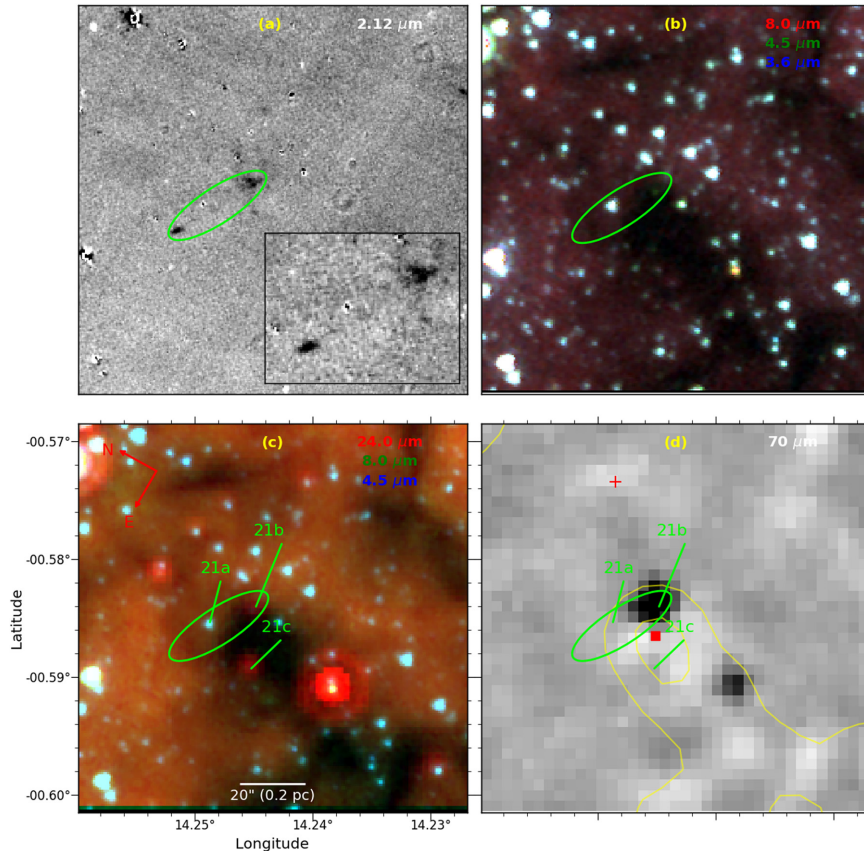


**Figure 3.** An example figure showing a multiwavelength view of the ISM around an MHO. (a) The continuum-subtracted  $\text{H}_2$  image, revealing the  $\text{H}_2$  jets. The inset figure shows the zoomed view of the jets. (b) *Spitzer*–IRAC colour-composite image (3.6- $\mu\text{m}$  in blue, 4.5- $\mu\text{m}$  in green and 8.0- $\mu\text{m}$  in red); used to search for enhanced 4.5- $\mu\text{m}$  emission such as is found in EGOs. (c) *Spitzer*–IRAC/MIPS composite-colour image (4.5- $\mu\text{m}$  in blue, 8- $\mu\text{m}$  in green and 24- $\mu\text{m}$  in red); used to unveil deeply embedded protostars. (d) The grey-scale unsharp-masked 70- $\mu\text{m}$  image; used in the search for early class 0 sources such as PACS bright red sources (see Appendix A). Green contours show the distribution of 870- $\mu\text{m}$  emission (from the ATLASGAL survey). The position of the outflow on the *Spitzer* and 70- $\mu\text{m}$  images is shown with an ellipse and the major axis of the ellipse indicates the likely flow direction.

uses a number of combinations of central star, disc, infalling envelope and bipolar cavity, for a reasonably large parameter space. While other techniques (e.g. colour–colour diagrams or spectral indices) can be useful in identifying the evolutionary class, SED models have the ability to infer physical information about young stars such as the total luminosity, stellar age and mass and accretion rates, accounting for the geometry of the disc and envelope. However, interpreting SEDs using radiative transfer codes is subject to degeneracies, which spatially resolved multiwavelength observations can overcome (e.g. see Samal et al. 2015). Thus, we fit SED models to only those candidate YSOs for which we have constraints on the 70- $\mu\text{m}$  flux along with the fluxes at shorter wavebands between 1.2 and 24- $\mu\text{m}$ .

For the SED fitting, we adopted a distance  $2 \pm 0.2$  kpc and a visual extinction ( $A_V$ ) in range 2–50 mag, with lower limit corresponding to the foreground extinction to M17 (e.g. Hoffmeister et al. 2008), while the upper limit is in line with typical maximum values found towards EGOs (e.g. Caratti o Garatti et al. 2015) and UCH II regions (e.g. Hanson, Luhman & Rieke 2002). While fitting model SEDs, we adopted errors of 10, 15 and 20 per cent, respectively, for the UKDIS, *Spitzer* and 70- $\mu\text{m}$  fluxes instead of formal photometric errors, in order to fit without any possible bias caused by underestimation of the flux uncertainties. Fig. 5 shows the model SEDs of 14 sources for which we have a reasonable number of data points between 1.2 and 70- $\mu\text{m}$ . As can be seen, although SED mod-

els show some degree of degeneracy, they appear to fit the data reasonably well. Barring source 26 (i.e. the driving source of MHO 2333), all the SED models clearly show rising SEDs up to 70- $\mu\text{m}$ , consistent with our earlier classification that the majority of them are protostars.

Like any other model, these models have their own sets of limitations. For example, these models do not account for interstellar radiation fields (IRSF), cold dust of the protostellar envelopes (i.e. dust below 30 K), stellar multiplicity, etc. The main objective here is not to provide a precise set of physical parameters for the YSOs but to find the range of a few key parameters from the models and then discuss the possible nature of the sources. To do so, we obtained physical parameters of the sources by adopting an approach similar to Robitaille et al. (2007), i.e. by considering those models satisfying  $\chi^2 - \chi_{\min}^2 \leq 2N_{\text{data}}$ , where  $\chi_{\min}^2$  is the goodness-of-fit parameter for the best-fitting model and  $N_{\text{data}}$  is the number of input observational data points. We then obtained the parameters from the weighted mean and standard deviation of these best-fitting models weighted by  $e^{-\chi^2/2}$  (e.g. Samal et al. 2012). These parameters are tabulated in Table 2, including the stellar mass ( $M_*$ ), stellar age ( $t_*$ ), disc mass ( $M_{\text{disc}}$ ) disc accretion rate ( $\dot{M}_{\text{disc}}$ ) and total luminosity ( $L_{\text{bol}}$ ) of each source. As per the models, the disc masses are in the range 0.003–0.14  $M_{\odot}$  with a median  $\sim 0.02 M_{\odot}$ , disc accretion rates are in the range  $0.08$ – $9.7 \times 10^{-7} M_{\odot} \text{ yr}^{-1}$  with a median

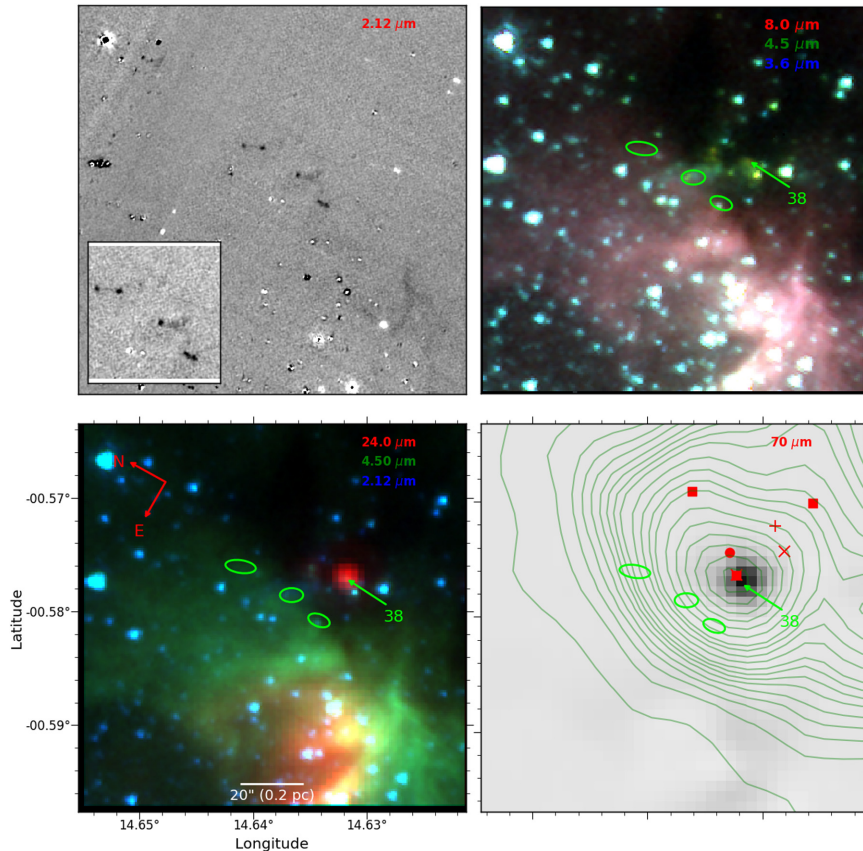


**Figure 4.** An example figure showing signs of star formation such as extended green emission, SiO maser ( $\times$ ), cold clumps from the ATLASGAL ( $\blacksquare$ ) and BGPS ( $\bullet$ ) surveys and IRDC fragments ( $+$ ) at the location of an outflow consisting of three jet-like structures (enclosed by oval-shaped marks). In this work, we have considered that the jets are part of a single outflow, the origin of which lies in the clump (see text for details). All the images have the same meaning as in Fig. 3.

$\sim 2.8 \times 10^{-7} M_{\odot} \text{ yr}^{-1}$  and age is in the range  $0.05\text{--}3 \times 10^5 \text{ yr}$  with a median value  $\sim 1 \times 10^5 \text{ yr}$ .

Fig. 6(a) shows the disc masses of the YSOs obtained in the present work (blue dots) and their comparison with those in the nearby star-forming regions (Williams & Cieza 2011), measured through sub(mm) observations. In Fig. 6(a), the solid line represents the median ratio of disc to stellar mass, i.e.  $\sim 1$  per cent as derived by Williams & Cieza (2011) from the compilation of a large number of class II/III YSOs in the stellar mass range  $0.4\text{--}10 M_{\odot}$ , and the shaded area represents the 1-dex spread about the median value of their sample. Similarly, Fig. 6(b) shows the disc accretion rates of the YSOs obtained in the present work (blue dots) and their comparison with the literature values of nearby star-forming regions as compiled by Hartmann, Herczeg & Calvet (2016). These authors compiled a large number of class II/III YSOs, for which accretion rates are measured in various ways (e.g. spectroscopic measurements of the Balmer continuum, photometric  $U$ -band measurements and emission-line measurements), and observed a strong correlation with stellar mass. In Fig. 6(b), the solid line represents the relation,  $\dot{M}_{\text{disc}} \propto M_{*}^{2.1}$ , obtained by Hartmann et al. (2016) and the shaded area represents the  $3\sigma$  scatter around this line, where  $\sigma$  is  $\sim 0.75$  dex (see Hartmann et al. 2016 for detailed discussion).

As can be seen from Fig. 6, despite the evolutionary differences between the sources (i.e. protostars versus class II/III YSOs), in general the SED model-based disc measurements show a fair agreement with the literature values at any given stellar mass, indicating that

the obtained disc properties of the driving sources may be a representation of their true values. In the absence of high-resolution mm observations and precise extinction measurements, we emphasize that the obtained disc parameters are still indicative and should be treated with caution. On the other hand, as one can see from Fig. 5, for a given source the overall shape of all models is similar in general, so bolometric luminosities of sources are expected to be better constrained. In fact, we find they are in reasonable agreement with luminosity estimated based on the  $70\text{-}\mu\text{m}$  flux alone (discussed in Section 4.2.2).

#### 4.2.2 Luminosity of the driving sources using only $70\text{-}\mu\text{m}$ flux

Dunham et al. (2006), using radiative transfer models, demonstrated that  $70\text{-}\mu\text{m}$  is a crucial wavelength for determining  $L_{\text{bol}}$  for embedded protostars, as radiative transfer models are strongly constrained by this wavelength and it is largely unaffected by the details of the source geometry and external heating. Furthermore, Dunham et al. (2008) examined c2d protostars and obtained the following tight correlation between  $L_{\text{bol}}$  (excluding luminosity arising from external heating) and  $F_{70}$  for low-luminosity protostars:

$$L_{\text{bol}} = 3.3 \times 10^8 F_{70}^{0.94} (d/140\text{pc})^2 L_{\odot}, \quad (1)$$

where  $F_{70}$  is in cgs units ( $\text{erg cm}^{-2} \text{ s}^{-1}$ ). While this method is accurate within a factor of 2–3 (e.g. Dunham et al. 2008; Commerçon et al. 2012), it offers a proxy way of obtaining  $L_{\text{bol}}$  for embedded

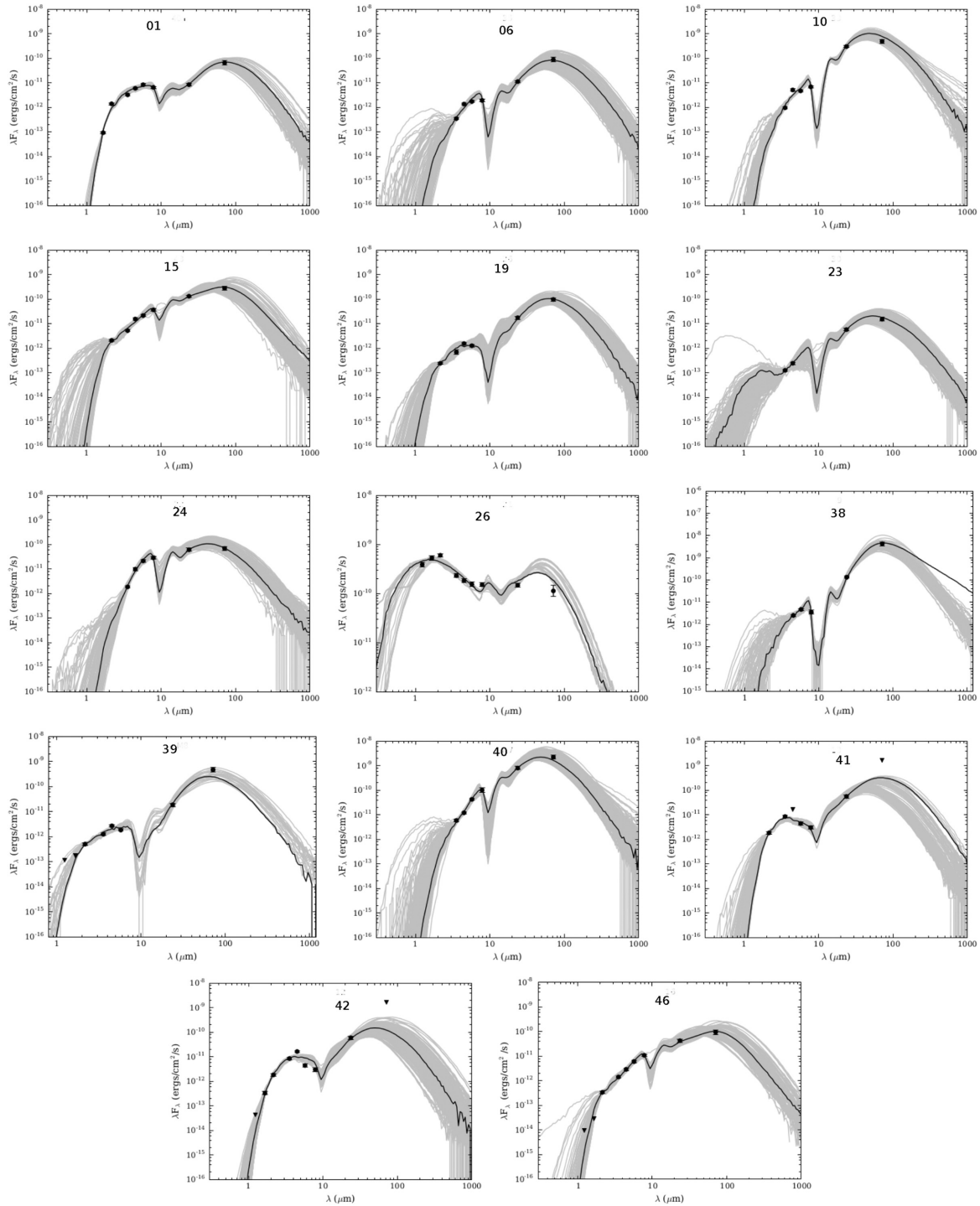


**Figure 5.** The observed SEDs of the driving sources and their best-fitting models. The ID numbers correspond to the entries in the first column of Table 1. The black line shows the best-fitting model and the grey-lines show subsequent best-fitting models that satisfy  $\chi^2 - \chi_{\min}^2 \leq 2N_{\text{data}}$  criteria. Filled circles and triangles show the ‘data points’ and ‘upper limits’ respectively. The IDs correspond to the MHO names given in Table 1.

protostars. It is worth noting that Ragan et al. (2012) have shown that the 70- $\mu\text{m}$  flux of more massive sources also correlates well with their total luminosity and there is good agreement between the correlations established for low- and high-luminosity sources. Among our YSO sample, five sources have detection only at 24 and 70- $\mu\text{m}$ , or at 70- $\mu\text{m}$ , for which we could not perform SED modelling. We therefore used the above empirical relationship for

obtaining the bolometric luminosity of these candidates. Of these, four are found to be in the range  $\sim 4\text{--}53 L_{\odot}$ , and one is exceptionally luminous, with luminosity  $\sim 0.5 \times 10^4 L_{\odot}$ . The latter source corresponds to an extremely young YSO associated with an EGO (see Section 5.1 for further discussion). The luminosity of these sources is also tabulated in Table 2. We compared the 70- $\mu\text{m}$  flux-based and SED model-based luminosities for common protostars

**Table 2.** Physical parameters inferred from the SED modelling.

ID	$M_*$ ( $M_\odot$ )	Age ( $10^5$ yr)	$M_{\text{disc}}$ ( $M_\odot$ )	$\dot{M}_{\text{disc}}$ ( $10^{-8} M_\odot \text{ yr}^{-1}$ )	$L$ ( $10^2 L_\odot$ )
01	$2.10 \pm 0.87$	$1.56 \pm 0.90$	$0.049 \pm 0.073$	$00.04 \pm 00.09$	$0.27 \pm 0.06$
06	$1.75 \pm 0.70$	$0.99 \pm 0.68$	$0.007 \pm 0.009$	$00.21 \pm 00.64$	$0.26 \pm 0.09$
10	$4.13 \pm 0.70$	$0.14 \pm 0.26$	$0.099 \pm 0.057$	$08.24 \pm 06.46$	$2.52 \pm 0.17$
15	$1.45 \pm 0.62$	$0.15 \pm 0.31$	$0.077 \pm 0.037$	$05.78 \pm 06.30$	$0.53 \pm 0.22$
19	$2.07 \pm 0.53$	$1.32 \pm 0.64$	$0.011 \pm 0.013$	$00.09 \pm 00.20$	$0.34 \pm 0.09$
23	$0.96 \pm 0.31$	$0.86 \pm 0.69$	$0.013 \pm 0.013$	$00.36 \pm 00.97$	$0.13 \pm 0.04$
24	$1.00 \pm 0.32$	$0.05 \pm 0.28$	$0.007 \pm 0.012$	$05.04 \pm 09.42$	$0.35 \pm 0.13$
26	$5.85 \pm 0.17$	$2.77 \pm 0.77$	$0.065 \pm 0.042$	$00.03 \pm 00.03$	$2.86 \pm 0.44$
38	$4.58 \pm 2.50$	$0.04 \pm 0.07$	$0.141 \pm 0.107$	$97.49 \pm 95.73$	$7.15 \pm 1.57$
39	$5.07 \pm 0.61$	$2.10 \pm 0.63$	$0.006 \pm 0.016$	$00.01 \pm 00.03$	$1.47 \pm 0.43$
40	$6.51 \pm 1.75$	$0.78 \pm 0.71$	$0.126 \pm 0.146$	$20.39 \pm 40.12$	$8.27 \pm 2.06$
41	$4.60 \pm 0.26$	$1.40 \pm 0.08$	$0.015 \pm 0.010$	$00.05 \pm 00.01$	$0.92 \pm 0.06$
42	$4.22 \pm 0.79$	$2.76 \pm 1.10$	$0.003 \pm 0.007$	$00.01 \pm 00.04$	$0.70 \pm 0.14$
46	$1.15 \pm 0.31$	$0.25 \pm 0.17$	$0.020 \pm 0.017$	$00.67 \pm 01.52$	$0.20 \pm 0.06$

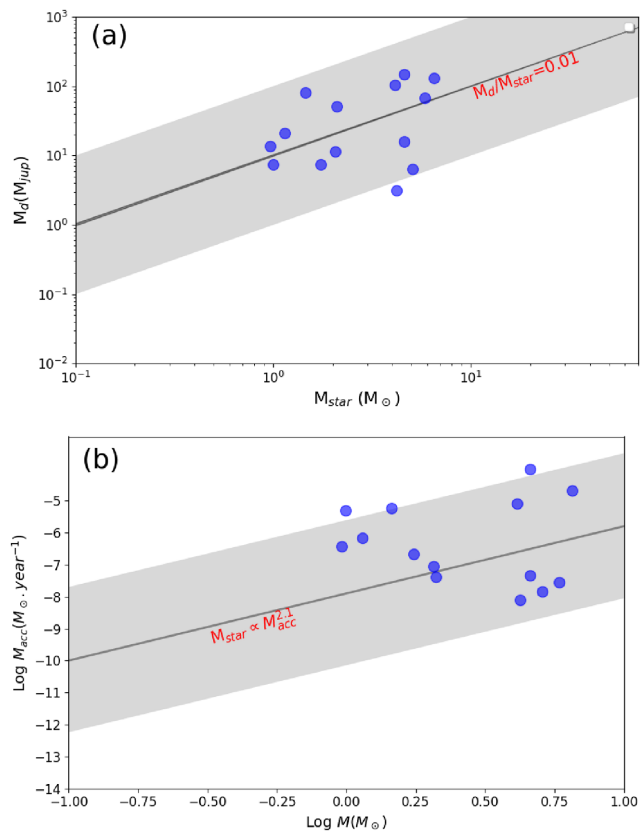


**Figure 6.** (a) Variation of protoplanetary disc mass (in units of Jupiter mass) with the mass of the central star. (b) Correlation between stellar mass and accretion rate. In both plots, our SED model-based measurements are shown as blue dots, while the solid line and the shaded area represent measurements from the literature for class II/III YSOs and have the same meaning as described in the text.

(i.e. class 0/I) and found that the two estimates are in agreement with each other within a factor of 2.

From the luminosity and disc properties of the driving sources, we can say that most of them are intermediate-mass young stellar objects (for the mass–luminosity relationship of protostars, see Fig. 4 of André et al. (2008) and references therein) that are still actively accreting from their protoplanetary disc. We note that outflow power

is strongly correlated to YSO luminosity (e.g. Caratti o Garatti et al. 2015), therefore the predominance of moderate-mass YSOs in our sample of driving sources could be a selection effect caused by the sensitivity of the *Spitzer* and *Herschel* images at the distance of M17.

## 5 DISCUSSION

### 5.1 Notes on the general nature of MHOs and discussion on a few types of interesting source

In this work, we have identified 48 MHOs, of which 45 (93 per cent) are new discoveries. Of the three already known outflows, two (MHO 2306 and MHO 2344) have been identified by Cyganowski et al. (2008) as EGOs using *Spitzer* observations and one (i.e. MHO 2307) by Caratti o Garatti et al. (2015) using 2.12- $\mu\text{m}$  observations. This shows the improvement UWISH2 can bring when it comes to identifying outflows over Galactic scales.

Out of 48 MHOs, we could only associate 20 YSO candidates. This corresponds to 40 per cent of all MHOs. If we consider dust cores and clusters as the potential driving sources, the number of sources increases to 30, which is  $\sim 60$  per cent of all MHOs. We could not link the remaining MHOs with any potential YSO candidates, which could be due to either indistinct shock orientation with respect to the nearby YSOs or shocks coming from distant sources or low-luminosity sources beyond our sensitivity limit ( $< 3 L_\odot$ ; discussed below). However, largely the situation here is similar to Serpens and Aquila (Ioannidis & Froebrich 2012a), Orion A (Davis et al. 2009), Vela C (Zhang, Wang & Henning 2014) and Cygnus-X (Makin & Froebrich 2018), where only 50 to 60 per cent of MHOs were found to have associated YSOs.

From SED models or using only 70- $\mu\text{m}$  fluxes, we find that outflows are driven mostly by sources of luminosity in the range 4–1000  $L_\odot$ , suggesting that more low- to intermediate-mass YSOs with outflows can be studied and characterized over larger distances with the help of the UWISH2 survey.

In our sample, six (MHO 2306, MHO 2328, MHO 2329, MHO 2331, MHO 2337 and MHO 2343) out of the 20 YSOs have no detection in 5.8- and/or 8.0- $\mu\text{m}$  bands in the MIPS GAL catalogue, yet were detected at 24 and/or 70- $\mu\text{m}$ . Our findings suggest that a search for outflow-driving sources without 24 and 70- $\mu\text{m}$  would result in missing many potential candidates (e.g.  $\sim 30$  per cent in the present case). 24- $\mu\text{m}$  is an important wavelength for determining

whether a source features a rising (or falling) SED. 70- $\mu\text{m}$  is particularly important for the identification of very young protostars and perhaps even the first hydrostatic cores (e.g. Enoch et al. 2010). We find, as protostars are bright in the mid- and far-infrared, that in the multi-colour IRAC–MIPS images the outflow-driving sources stand out clearly compared with nearby sources (e.g. see the figures in Appendix B).

In our sample (see Table 1), although the majority of bipolar outflows have a total length less than 0.4 pc, the MHO 2347 corresponds to a parsec-scale outflow (see Fig. 7) from a class 0 source. We note that Caratti o Garatti et al. (2015) have also observed MHO 2347, but only part of it. With our sensitive observations, we detect an additional three knots along the south-western lobe of MHO 2347, which makes it the largest  $\text{H}_2$  outflow of the M17 complex. We find that the outflow shows some degree of bend morphology and consists of a series of compact knots at a median spacing of  $\sim 0.15$  pc (for details see Appendix B). Episodic ejection of material by quasi-periodic outbursts of the central star–disc system is one of the possible explanations for regular spacing between the knots (e.g. Raga, Riera & González-Gómez 2010). Recently, Vorobyov & Basu (2015), using hydrodynamical simulations, showed that episodic accretion events induced by gravitational instabilities and disc fragmentation are present mainly during the early evolution (class 0) of most protostellar systems. In addition to bursts induced by disc instabilities, it has also been suggested that bursts can be induced by external interactions with one or more companion stars. Objects like MHO 2347 are therefore of particular interest for studying the accretion history and cause of variability in very young systems (e.g. see the discussion in Caratti o Garatti et al. 2017; Herczeg et al. 2017; Meyer et al. 2017).

In our list, we find that MHO 2306 corresponds to an EGO (details given in Appendix B). This MHO has been identified by Lee et al. (2012) using UWISH2 images while searching for EGO counterpart in  $\text{H}_2$ . We find a bright 70- $\mu\text{m}$  point source at the location of the EGO. The source location also coincides with the location of a methanol maser (Bayandina, Val'ts & Larionov 2012), which is a tracer of early evolutionary stages of high-mass star formation (Ellingsen 2006). The source lies adjacent to a compact  $\text{H II}$  region that is bright at 8 and 24- $\mu\text{m}$  (see Fig. 8) and has no 24- $\mu\text{m}$  counterpart in the MIPS GAL catalogue. It is embedded in a clump of column density  $\sim 7 \times 10^{23} \text{ cm}^{-2}$  (Tang et al. 2017), thus in a region of very high extinction. Its 70- $\mu\text{m}$  flux suggests a source of luminosity  $\sim 0.5 \times 10^4 L_{\odot}$ ; however, no associated radio free-free emission at 5 GHz (resolution  $\sim 1.5$  arcsec and rms  $\sim 0.4$  mJy) is found in the CORNISH<sup>6</sup> survey image (Hoare et al. 2012). It appears that, although its luminosity represents a high-mass star, it is yet to develop an UCH II region. Thus it represents a young massive YSO with an outflow. Similarly, MHO 2344 (driven by a  $\sim 700 L_{\odot}$  class 0 type YSO) presents a case where multiple wide-angle bullets have been observed (see Fig. 4 and Section 4.1 for details). We suggest that these massive YSOs are potential candidates for studying various aspects of the early phases of massive star formation and evolution (e.g. see the discussion in Tan et al. 2016; Bally et al. 2017).

We identified  $\text{H}_2$  jets and knots in the vicinity of six 70- $\mu\text{m}$  dark cores (MHO 2335, MHO 2338, MHO 2341, MHO 2350, MHO 2352 and MHO 2353), but for three cases (MHO 2341, MHO 2350 and MHO 2352) we observed symmetric jets clearly emanating from the cores located in the middle of the jet axis. Fig. 9 illustrates an

example. As can be seen, the MHO consists of two strong opposite jets. Together, they delineate a north–south outflow. In the *Spitzer* bands, a dark cloud perpendicular to the flow axis can be seen as an absorption feature against the bright background. The morphology and the compactness of the jets strongly suggest that a driving source should be embedded inside the dark cloud. No point sources were found between 3.6 and 70- $\mu\text{m}$  in the dark cloud along the axis of the jets. However, one can see that a SCUBA core (mass  $\sim 9 M_{\odot}$ ; Reid & Wilson 2006) lies at the expected location. Thus, the core is the most likely source responsible for the jets. Most of the driving sources identified in this work are bright in the mid-infrared and visible at 70- $\mu\text{m}$ . The  $3\sigma$  point-source sensitivity of the 70- $\mu\text{m}$  image is  $\sim 0.24$  Jy, where  $\sigma$  is the standard deviation of the background intensity. Using equation (1), 0.24 Jy corresponds to a luminosity  $\sim 3 L_{\odot}$ . Thus, we cannot ignore the possibility that the starless cores may in fact harbour faint YSOs of luminosity  $< 3 L_{\odot}$ . At this point, we are ill-qualified to comment whether these 70- $\mu\text{m}$  dark cores are starless or protostellar. None the less, these mid- and far-infrared quiet clumps/cores are potential targets for understanding the early phases of core collapse and fragmentation (e.g. see the discussion in Palau et al. 2018; Traficante et al. 2018).

## 5.2 Dominant YSO class responsible for the jets

The present  $\text{H}_2$  survey cover a small area about  $1.5 \text{ deg}^2$ , but it is worthwhile comparing our results with the results from other similar surveys of nearby star-forming regions to understand at what stage of protostellar evolution  $\text{H}_2$  jets are prominent. In the present work, we find that, of the 20 YSOs with outflows, 18 ( $\sim 90$  per cent) are driven by protostars (i.e. class 0/I YSOs), which is similar to the  $\geq 80$  per cent of the  $\text{H}_2$  outflows in Orion A (Davis et al. 2009),  $\sim 90$  per cent in Corona Australis (Kumar et al. 2011),  $\geq 90$  per cent in Serpens South (Teixeira et al. 2012),  $\sim 70$  per cent in Aquila (Zhang et al. 2015) and  $\sim 80$  per cent in Cygnus-X (Makin & Froebrich 2018) molecular clouds, with the exception of the Cassiopeia and Auriga complex (Froebrich & Makin 2016), where 20 per cent of the driving sources are protostars; the remainder are classical T Tauri stars. The above trend (except for the Cassiopeia and Auriga complex) hints that  $\text{H}_2$  jets are mostly prominent in class 0/I type protostars and the jet activity possibly decreases significantly as the object evolves. However, we stress that the above trend could be biased by the selection effect, as older sources tend to reside in relatively molecule-free environments and thus their shocks may not be traced by MHOs. Sensitive optical observations of  $\text{H}\alpha$  and [S II] lines would be helpful to solidify the above trend.

## 5.3 Jet lengths and dynamical time-scales

Fig. 10 shows the frequency distribution of the total length of the outflows associated with either a YSO or a core. Here, we assume that the total length of a monopolar appearance outflow is twice its single-sided lobe length (the distance of the furthest  $\text{H}_2$  feature from the YSO/core), while it is end-to-end for bipolar outflows. Using this simple approach, we find that the total outflow lengths of the MHOs are in the range 0.05–1.2 pc, with a median  $\sim 0.34$  pc.

We note that these lengths refer to the lengths of the visible  $\text{H}_2$  jets, not necessarily the total lengths of the flows, as outflow length depends on many factors, such as the tracer in question, inclination angle to the line of sight, density of the ambient medium, etc., so more extreme values may be feasible. Froebrich & Makin (2016) argued that, since bipolar outflows are often asymmetric, measuring outflow lengths in the traditional way (from end to end) should be

<sup>6</sup><http://cornish.leeds.ac.uk/public/index.php>

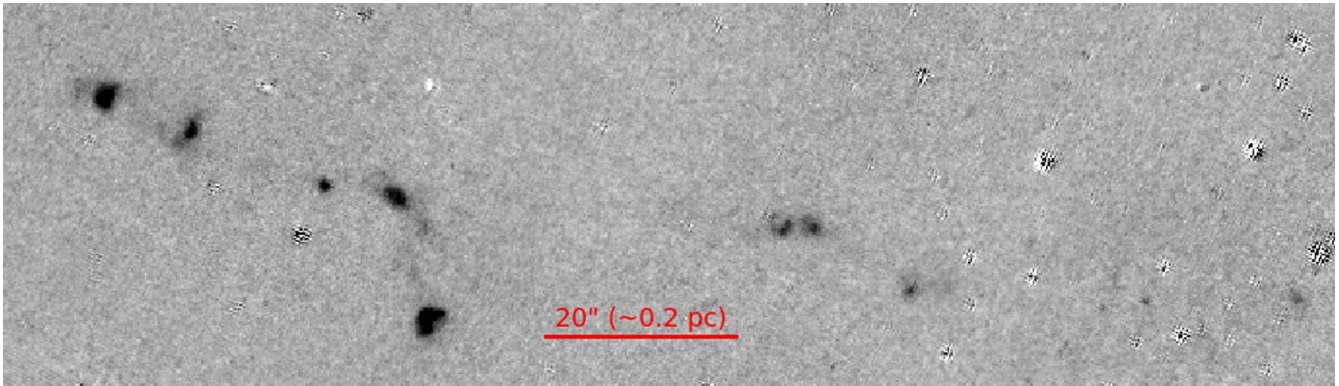


**Figure 7.** Continuum-subtracted  $\text{H}_2$  image of MHO 2347, showing a chain of knots spread over the parsec-scale. We note that the bright bow-shock-shaped knot seen in the central bottom part of the figure is part of MHO 2307.

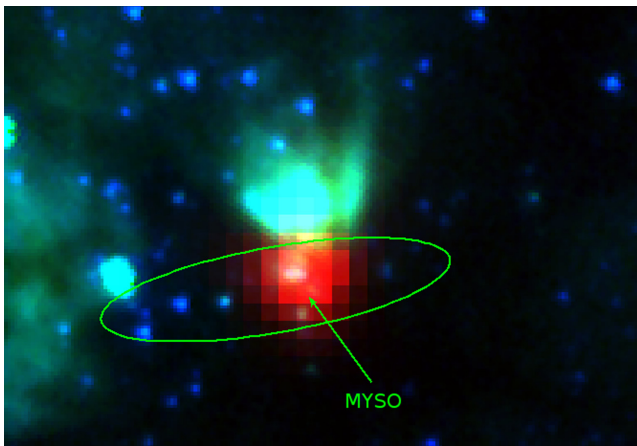


**Figure 8.** Colour-composite image around MHO 2306 at 3.6 (blue), 8.0 (green) and 70- $\mu\text{m}$  (red). The ellipse denotes the flow axis of MHO 2306 (for details see Appendix B). The arrow points to the 70- $\mu\text{m}$  bright MYSO, the likely source responsible for MHO 2306.

avoided. Owing to low statistics of the outflow sources, here we did not measure the length of each lobe separately. None the less, if we consider the length of the longest lobe as the true half-length of a bipolar flow, then we find that the total outflow lengths of all MHOs are in the range 0.09–1.6 pc, with median  $\sim 0.44$  pc. We point out that outflows can break out of their parent clumps and interact with a medium with little molecular gas; thus, the MHO-based outflow sizes could be limited by the spatial extent of the molecular cloud and hence are likely representative of lower bounds of the true extent of the flows. We estimated the likely lower limits of the dynamical time-scales ( $t_{\text{dyn}}$ ) of the outflows using the relation  $t_{\text{dyn}} = D/(V \sin i)$ , where  $D$  is the length of the lobe,  $V$  is the velocity of the jet and  $i$  is the inclination of the outflow with respect to the line of sight. Here we assume an average flow inclination angle  $\sim 57^\circ.3$  (see the discussion in Bontemps et al. 1996), a flow velocity  $\sim 35 \text{ km s}^{-1}$  which is the median value of 86  $\text{H}_2$  features measured by Zhang et al. (2013) using proper motion observations, and that jets travel with a constant velocity since their launch. Under these assumptions, we find that the time-scales of ejection are in the range  $0.01\text{--}0.2 \times 10^5 \text{ yr}$ , with median  $\sim 0.07 \times 10^5 \text{ yr}$ . The median time-scale is slightly lower than the lifetime of the class 0/I sources ( $\sim 0.4 \times 10^5 \text{ yr}$ ; Evans et al. 2009) and the median age of the YSOs as estimated from SED modelling. Proper velocity and size measurements and inclination

angle of the jets would shed more light on the correlation between the dynamical time-scale and the lifetime of protostars.

## 6 GENERAL PICTURE OF STAR FORMATION IN THE M17 COMPLEX

As discussed in Section 5.2, jets are possibly more prominent in the class 0/I phase of a YSO. Thus the distribution of  $\text{H}_2$  jets/knots offers an independent diagnostic to trace the recent star formation activity of a complex. Fig. 2(a) shows the relative spatial distribution of MHOs and the cold gas at 870- $\mu\text{m}$ . As can be seen, the cold dust emission (red contours) corresponds mainly to the absorption features of the background 24- $\mu\text{m}$  image and is concentrated primarily at the location of the A, B, C and D components of the complex. Also, most of the MHOs are located in the close vicinity of the intense 870- $\mu\text{m}$  emission and show a good correlation with the distribution of SiO emission. We observed that, in 70 per cent of the cases, the clump with SiO emission coincides with an MHO, suggesting that active star formation is ongoing in these clumps. Looking at the large-scale spatial distribution of MHOs and 870- $\mu\text{m}$  dust emission, it appears that the M17 complex consists of several scattered star-forming clumps with jets and SiO emission, separated by distances of several pc from each other. This suggests the hierarchical nature of the molecular cloud (e.g. see the discussion in Vázquez-Semadeni, González-Samaniego & Colín 2017; Caldwell & Chang 2018).

One can also notice that, among the structures of M17, M17SWex is filamentary and  $\text{H}_2$  flows are more abundant in its direction compared with other parts of the complex. Using high-resolution  $\text{NH}_3$  and 1.3-mm observations, dense filamentary clouds with density as high as  $\sim 10^{23} \text{ cm}^{-2}$  have been observed in M17SWex (Busquet et al. 2013, 2016). This high column of matter could have limited our ability to detect some of the weaker flows compared with the less extinguished regions of the complex. Even so, based on the distribution of MHOs, it appears largely that M17SWex is currently forming stars actively among all fragments, thereby supporting the fact that in molecular clouds filaments and filamentary structures are prime sites of active star formation (e.g. Könyves et al. 2015; Samal et al. 2015; Ryabukhina et al. 2018). We find that our results are in accordance with the results obtained by Povich & Whitney (2010), Busquet et al. (2013), Busquet et al. (2016) and Povich et al. (2016) and for M17SWex. These authors, using multiwavelength observations, found that the M17SWex region is associated with a rich number of YSOs/cores and suggest that it may form many more

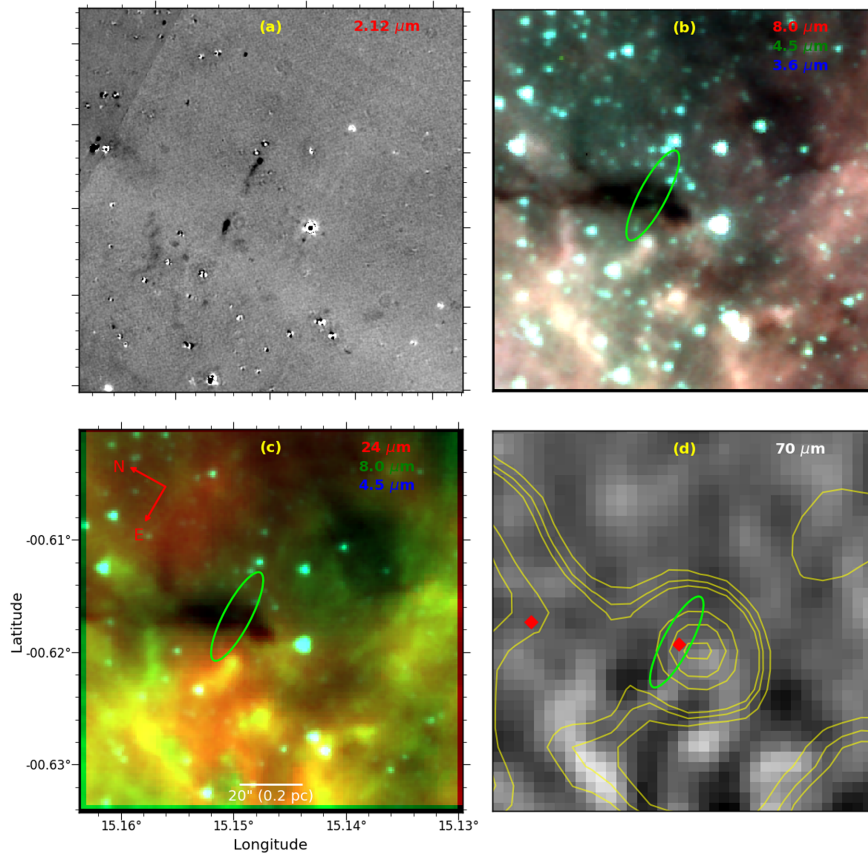


**Figure 9.** Multicolour image around MHO 2352, showing the emergence of  $\text{H}_2$  jets from a *Spitzer* dark cloud, with no embedded point sources up to 70- $\mu\text{m}$ . The colour codings have the same meaning as in Fig. 3. The diamond symbols on the 70- $\mu\text{m}$  image represent the SCUBA cores. The 870- $\mu\text{m}$  contours are shown in orange colours.

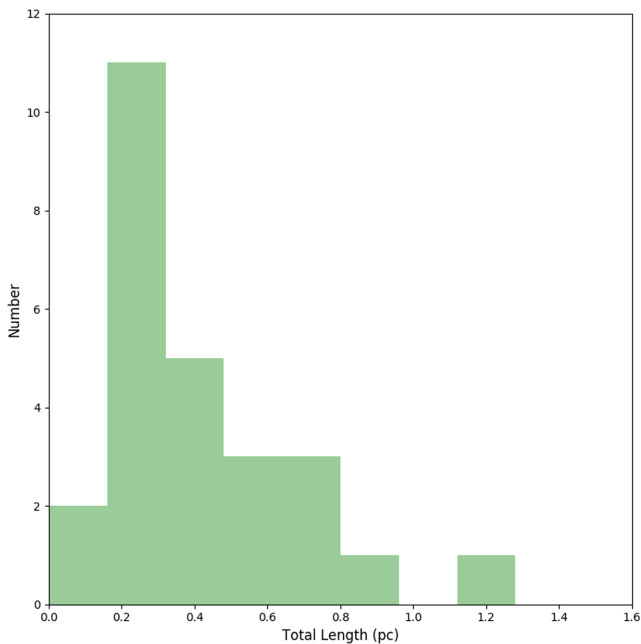


**Figure 10.** Total length distribution of the outflows that are associated with either a YSO or a core.

stars by accreting a significant amount of the surrounding gas fed by the filaments.

In contrast to M17SWex, in the interior of the  $\text{H}_{\text{II}}$  region, we observed only a few MHOs – which is not surprising, given the fact that it hosts a 3-Myr-old cluster (the cluster centre is marked with a star symbol in the figure), where one would expect a low fraction of sources with active accretion disc (e.g. Jose et al. 2017). This implies that star formation has stopped or is in a more advanced phase in the central region of M17. The presence of a significant amount of 870- $\mu\text{m}$  cold dust and a small number of outflows (either MHOs or SiO emission) surrounding the  $\text{H}_{\text{II}}$  region (particularly in the fragment ‘B’), however, suggests that a very early phase of star formation is still ongoing at the periphery of the  $\text{H}_{\text{II}}$  region. We suggest that these outflows are probably from the second-generation young stars, formation of which has been triggered by the compression of the expanding  $\text{H}_{\text{II}}$  region, as observed at the borders of several Galactic  $\text{H}_{\text{II}}$  regions (e.g. Getman et al. 2012; Panwar et al. 2014; Samal et al. 2014; Deharveng et al. 2015; Bernard et al. 2016). In fact, strong evidence that M17SW and nearby molecular clouds are heated and compressed by the  $\text{H}_{\text{II}}$  region has been observed using molecular observations (e.g. Lada 1976; Wilson, Hanson & Muters 2003).

All in all, in the M17 complex, M17SWex appears to be the most active site of star formation, representing an excellent cloud for understanding the early phases of cluster formation and evolution under the influence of strong outflow feedback.

## 7 SUMMARY

In this work, we use infrared observations of the H<sub>2</sub> 1–0 S(1) line at 2.12- $\mu$ m, with UKIDSS, *Spitzer* and *Herschel* maps in the wavelength range 1.2–70- $\mu$ m, to identify protostars with jets and knots in the M17 complex as well as to understand its ongoing star formation activity.

We identified 48 MHOs over a  $2.0^\circ \times 0.8^\circ$  area of the complex, i.e. potential outflow candidates,  $\sim 93$  per cent of which are new discoveries. Based on the alignments and morphologies of the MHOs with the nearby YSO candidates, we could associate 20 YSO candidates with the outflows. Using various flux ratios, we deduce an evolutionary status of these candidates and find that  $\sim 90$  per cent of the driving sources are protostars (i.e. class 0/I) and only  $\sim 10$  per cent of the MHOs are driven by class II YSOs. Among the protostars, three are likely PBRs.

Using the grid models of Robitaille et al. (2006), we matched the model spectral energy distributions to the observed SEDs of the 14 outflow-driving YSOs. This allows for an estimation of the physical properties such as mass, luminosity and accretion rate of the protostars. We find that the disc masses and disc accretion rates of  $\sim 80$  per cent of YSOs are in the range  $0.003\text{--}0.14 M_\odot$  and  $0.08\text{--}9.7 \times 10^{-7} M_\odot \text{ yr}^{-1}$ , respectively. From SED modelling and using only 70- $\mu$ m flux, we estimated that the outflows are mostly driven by sources of luminosity in the range  $4\text{--}1000 L_\odot$ , suggesting that more low- to intermediate-mass YSOs with outflows can be studied and characterized over larger distances with the help of the UWISH2 survey.

Our results show that six outflows are possibly emanating from cores where no infrared sources were detected up to 70- $\mu$ m. These sources are important targets for follow-up studies to understand the very early phase of star formation.

We observed a pc-scale bipolar outflow from a class 0 YSO with regularly spaced knots, a potential candidate for understanding the variability in very young systems. We also observed a strong spatial correlation between H<sub>2</sub> jets/knots and SiO emission for massive ATLASGAL clumps.

Among the structures of M17, we find that H<sub>2</sub> jets/knots are statistically more numerous in the M17SWex region of the complex. Since H<sub>2</sub> emission is a tracer of recent ejecta from young protostars, we suggest that, in the M17 complex, currently M17SWex is the most active region of star formation and is an excellent template for understanding the early evolution of young clusters that are under the influence of strong outflow feedback.

## ACKNOWLEDGEMENTS

We are grateful to the anonymous referee for useful comments that have helped us to improve the scientific contents of the article. MRS acknowledges the Ministry of Science and Technology of Taiwan for his post-doctoral fellowship. The data reported here were obtained as part of the UKIRT Service Program.

## REFERENCES

Aguirre J. E. et al., 2011, *ApJS*, 192, 4  
 Allen L. E. et al., 2004, *ApJS*, 154, 363  
 André P. et al., 2008, *A&A*, 490, L27  
 Arce H. G., Shepherd D., Gueth F., Lee C.-F., Bachiller R., Rosen A., Beuther H., 2007, *Protostars and Planets V*, p. 245  
 Aso Y. et al., 2017, *ApJ*, 850, L2  
 Bally J., 2007, *Ap&SS*, 311, 15

Bally J., Cunningham N. J., Moeckel N., Burton M. G., Smith N., Frank A., Nordlund A., 2011, *ApJ*, 727, 113  
 Bally J., Ginsburg A., Arce H., Eisner J., Youngblood A., Zapata L., Zinnecker H., 2017, *ApJ*, 837, 60  
 Bally J., Ginsburg A., Probst R., Reipurth B., Shirley Y. L., Stringfellow G. S., 2014, *AJ*, 148, 120  
 Bally J., Ginsburg A., Silvia D., Youngblood A., 2015, *A&A*, 579, A130  
 Balog Z. et al., 2014, *Experimental Astronomy*, 37, 129  
 Bayandina O. S., Val'ts I. E., Larionov G. M., 2012, *Astron. Rep.*, 56, 553  
 Benjamin R. A. et al., 2003, *PASP*, 115, 953  
 Bernard A., Neichel B., Samal M. R., Zavagno A., Andersen M., Evans C. J., Plana H., Fusco T., 2016, *A&A*, 592, A77  
 Bhavya B., Subramaniam A., Kuriakose V. C., 2013, *MNRAS*, 435, 663  
 Bontemps S., André P., Terebey S., Cabrit S., 1996, *A&A*, 311, 858  
 Broos P. S. et al., 2013, *ApJS*, 209, 32  
 Busquet G. et al., 2013, *ApJ*, 764, L26  
 Busquet G. et al., 2016, *ApJ*, 819, 139  
 Cabrit S., 2007, in Bouvier J., Appenzeller I., eds, *IAU Symposium Vol. 243, Star–Disk Interaction in Young Stars*, p. 203  
 Caldwell S., Chang P., 2018, *MNRAS*, 474, 4818  
 Caratti o Garatti A., Stecklum B., Linz H., Garcia Lopez R., Sanna A., 2015, *A&A*, 573, A82  
 Caratti o Garatti A. et al., 2017, *Nature Physics*, 13, 276  
 Carey S. J. et al., 2009, *PASP*, 121, 76  
 Carney M. T., Yildiz U. A., Mottram J. C., van Dishoeck E. F., Ramchandani J., Jørgensen J. K., 2016, *A&A*, 586, A44  
 Chapman N. L., Mundy L. G., Lai S.-P., Evans N. J., II, 2009, *ApJ*, 690, 496  
 Chini R., Elsaesser H., Neckel T., 1980, *A&A*, 91, 186  
 Codella C., Cabrit S., Gueth F., Cesaroni R., Bacciotti F., Lefloch B., McCaughrean M. J., 2007, *A&A*, 462, L53  
 Commerçon B., Launhardt R., Dullemond C., Henning T., 2012, *A&A*, 545, A98  
 Crapsi A., van Dishoeck E. F., Hogerheijde M. R., Pontoppidan K. M., Dullemond C. P., 2008, *A&A*, 486, 245  
 Csengeri T. et al., 2014, *A&A*, 565, A75  
 Csengeri T. et al., 2016, *A&A*, 586, A149  
 Cyganowski C. J., Brogan C. L., Hunter T. R., Churchwell E., 2009, *ApJ*, 702, 1615  
 Cyganowski C. J. et al., 2008, *AJ*, 136, 2391  
 Davis C. J., Gell R., Khanzadyan T., Smith M. D., Jenness T., 2010, *A&A*, 511, A24  
 Davis C. J., Kumar M. S. N., Sandell G., Froebrich D., Smith M. D., Currie M. J., 2007, *MNRAS*, 374, 29  
 Davis C. J. et al., 2009, *A&A*, 496, 153  
 De Buizer J. M., Vacca W. D., 2010, *AJ*, 140, 196  
 Deharveng L. et al., 2015, *A&A*, 582, A1  
 Dunham M. M., Crapsi A., Evans N. J., II, Bourke T. L., Huard T. L., Myers P. C., Kauffmann J., 2008, *ApJS*, 179, 249  
 Dunham M. M. et al., 2006, *ApJ*, 651, 945  
 Dunham M. M. et al., 2015, *ApJS*, 220, 11  
 Ellingsen S. P., 2006, *ApJ*, 638, 241  
 Elmegreen B. G., Lada C. J., Dickinson D. F., 1979, *ApJ*, 230, 415  
 Enoch M. L., Evans N. J., II, Sargent A. I., Glenn J., 2009, *ApJ*, 692, 973  
 Enoch M. L., Lee J.-E., Harvey P., Dunham M. M., Schnee S., 2010, *ApJ*, 722, L33  
 Evans N. J., II et al., 2009, *ApJS*, 181, 321  
 Feng S., Beuther H., Zhang Q., Liu H. B., Zhang Z., Wang K., Qiu K., 2016, *ApJ*, 828, 100  
 Froebrich D., Makin S. V., 2016, *MNRAS*, 462, 1444  
 Froebrich D. et al., 2011, *MNRAS*, 413, 480  
 Froebrich D. et al., 2015, *MNRAS*, 454, 2586  
 Georgelin Y. M., Georgelin Y. P., Roux S., 1973, *A&A*, 25, 337  
 Gerin M., Pety J., Fuente A., Cernicharo J., Commerçon B., Marcelino N., 2015, *A&A*, 577, L2  
 Getman K. V., Feigelson E. D., Sicilia-Aguilar A., Broos P. S., Kuhn M. A., Garmire G. P., 2012, *MNRAS*, 426, 2917  
 Gibb A. G., Richer J. S., Chandler C. J., Davis C. J., 2004, *ApJ*, 603, 198  
 Guesten R., Fiebig D., 1988, *A&A*, 204, 253

- Gutermuth R. A., Heyer M., 2015, *AJ*, 149, 64
- Gutermuth R. A., Megeath S. T., Myers P. C., Allen L. E., Pipher J. L., Fazio G. G., 2009, *ApJS*, 184, 18
- Gutermuth R. A. et al., 2008, *ApJ*, 674, 336
- Hanson M. M., Luhman K. L., Rieke G. H., 2002, *ApJS*, 138, 35
- Hartmann L., Calvet N., Gullbring E., D'Alessio P., 1998, *ApJ*, 495, 385
- Hartmann L., Herczeg G., Calvet N., 2016, *ARA&A*, 54, 135
- Heiderman A., Evans N. J., II, 2015, *ApJ*, 806, 231
- Helfand D. J., Becker R. H., White R. L., Fallon A., Tuttle S., 2006, *AJ*, 131, 2525
- Herczeg G. J. et al., 2017, *ApJ*, 849, 43
- Hoare M. G. et al., 2012, *PASP*, 124, 939
- Hodapp K. W., 2007, *AJ*, 134, 2020
- Hoffmeister V. H., Chini R., Scheyda C. M., Schulze D., Watermann R., Nürnberger D., Vogt N., 2008, *ApJ*, 686, 310
- Hosokawa T., Omukai K., 2009, *ApJ*, 691, 823
- Ioannidis G., Froebrich D., 2012a, *MNRAS*, 421, 3257
- Ioannidis G., Froebrich D., 2012b, *MNRAS*, 425, 1380
- Jiang Z. et al., 2002, *ApJ*, 577, 245
- Joncas G., Roy J.-R., 1986, *ApJ*, 307, 649
- Jose J., Herczeg G. J., Samal M. R., Fang Q., Panwar N., 2017, *ApJ*, 836, 98
- Khazadyan T. et al., 2012, *A&A*, 542, A111
- Kumar M. S. N., Sharma S., Davis C. J., Borissova J., Grave J. M. C., 2011, *A&A*, 533, A137
- Könyves V. et al., 2015, *A&A*, 584, A91
- Lada C. J., 1976, *ApJS*, 32, 603
- Lada C. J., 1987, in Peimbert M., Jugaku J., eds, IAU Symposium Vol. 115, Star Forming Regions. p. 1
- Lee H.-T., Takami M., Duan H.-Y., Karr J., Su Y.-N., Liu S.-Y., Froebrich D., Yeh C. C., 2012, *ApJS*, 200, 2
- Lucas P. W. et al., 2008, *MNRAS*, 391, 136
- López-Sepulcre A., Watanabe Y., Sakai N., Furuya R., Saruwatari O., Yamamoto S., 2016, *ApJ*, 822, 85
- Makin S. V., Froebrich D., 2018, *ApJS*, 234, 8
- Manoj P. et al., 2013, *ApJ*, 763, 83
- Manoj P. et al., 2016, *ApJ*, 831, 69
- Meyer D. M.-A., Vorobyov E. I., Kuiper R., Kley W., 2017, *MNRAS*, 464, L90
- Molinari S. et al., 2010, *A&A*, 518, L100
- Noriega-Crespo A. et al., 2004, *ApJS*, 154, 352
- Palau A. et al., 2018, *ApJ*, 855, 24
- Panwar N., Chen W. P., Pandey A. K., Samal M. R., Ogura K., Ojha D. K., Jose J., Bhatt B. C., 2014, *MNRAS*, 443, 1614
- Pezzuto S. et al., 2012, *A&A*, 547, A54
- Plunkett A. L., Arce H. G., Corder S. A., Mardones D., Sargent A. I., Schnee S. L., 2013, *ApJ*, 774, 22
- Povich M. S., Townsley L. K., Robitaille T. P., Broos P. S., Orbin W. T., King R. R., Naylor T., Whitney B. A., 2016, *ApJ*, 825, 125
- Povich M. S., Whitney B. A., 2010, *ApJ*, 714, L285
- Povich M. S. et al., 2007, *ApJ*, 660, 346
- Povich M. S. et al., 2009, *ApJ*, 696, 1278
- Povich M. S. et al., 2013, *ApJS*, 209, 31
- Raga A. C., Riera A., González-Gómez D. I., 2010, *A&A*, 517, A20
- Ragan S. et al., 2012, *A&A*, 547, A49
- Ramos-Larios G., Guerrero M. A., Sabin L., Santamaría E., 2017, *MNRAS*, 470, 3707
- Ray T. P., 2007, in Bouvier J., Appenzeller I., eds, IAU Symposium Vol. 243, Star-Disk Interaction in Young Stars. p. 183
- Reach W. T. et al., 2006, *AJ*, 131, 1479
- Rebull L. M. et al., 2011, *ApJS*, 193, 25
- Reid M. A., Wilson C. D., 2006, *ApJ*, 644, 990
- Robitaille T. P., Whitney B. A., Indebetouw R., Wood K., 2007, *ApJS*, 169, 328
- Robitaille T. P., Whitney B. A., Indebetouw R., Wood K., Denzmore P., 2006, *ApJS*, 167, 256
- Rosolowsky E. et al., 2010, *ApJS*, 188, 123
- Ryabukhina O. L., Zinchenko I. I., Samal M. R., Zemlyanukha P. M., Ladeyschikov D. A., Sobolev A. M., Henkel C., Ojha D. K., 2018, *A&A*, preprint ([arXiv:1802.08030](https://arxiv.org/abs/1802.08030))
- Sahai R., Claussen M., Sánchez Contreras C., Morris M., Sarkar G., 2008, *ApJ*, 680, 483
- Sahai R., Lee C.-F., Sánchez Contreras C., Patel N., Morris M. R., Claussen M., 2017, *ApJ*, 850, 158
- Samal M. R., Pandey A. K., Ojha D. K., Chauhan N., Jose J., Pandey B., 2012, *ApJ*, 755, 20
- Samal M. R. et al., 2014, *A&A*, 566, A122
- Samal M. R. et al., 2015, *A&A*, 581, A5
- Stanke T., McCaughrean M. J., Zinnecker H., 2002, *A&A*, 392, 239
- Stutz A. M. et al., 2013, *ApJ*, 767, 36
- Tafalla M., Bachiller R., Lefloch B., Rodríguez-Fernández N., Codella C., López-Sepulcre A., Podio L., 2015, *A&A*, 573, L2
- Takami M., Chen H.-H., Karr J. L., Lee H.-T., Lai S.-P., Minh Y.-C., 2012, *ApJ*, 748, 8
- Takami M., Karr J. L., Koh H., Chen H.-H., Lee H.-T., 2010, *ApJ*, 720, 155
- Takami M., Karr J. L., Nisini B., Ray T. P., 2011, *ApJ*, 743, 193
- Tang X. D. et al., 2017, *A&A*, 598, A30
- Tan J. C., Kong S., Zhang Y., Fontani F., Caselli P., Butler M. J., 2016, *ApJ*, 821, L3
- Teixeira G. D. C., Kumar M. S. N., Bachiller R., Grave J. M. C., 2012, *A&A*, 543, A51
- Thronson H. A., Jr, Lada C. J., 1983, *ApJ*, 269, 175
- Traficante A., Fuller G. A., Smith R. J., Billot N., Duarte-Cabral A., Peretto N., Molinari S., Pineda J. E., 2018, *MNRAS*, 473, 4975
- Umamoto T. et al., 2017, *PASJ*, 69, 78
- Vorobyov E. I., Basu S., 2015, *ApJ*, 805, 115
- Vázquez-Semadeni E., González-Samaniego A., Colín P., 2017, *MNRAS*, 467, 1313
- Weingartner J. C., Draine B. T., 2001, *ApJ*, 548, 296
- Whitney B. A., Wood K., Bjorkman J. E., Cohen M., 2003b, *ApJ*, 598, 1079
- Whitney B. A., Wood K., Bjorkman J. E., Wolff M. J., 2003a, *ApJ*, 591, 1049
- Williams J. P., Cieza L. A., 2011, *ARA&A*, 49, 67
- Wilson T. L., Hanson M. M., Muders D., 2003, *ApJ*, 590, 895
- Wu Y. W. et al., 2014, *A&A*, 566, A17
- Zhang M., Fang M., Wang H., Sun J., Wang M., Jiang Z., Anathipindika S., 2015, *ApJS*, 219, 21
- Zhang M., Wang H., Henning T., 2014, *AJ*, 148, 26
- Zhang M. et al., 2013, *A&A*, 553, A41
- Zinchenko I., Liu S.-Y., Su Y.-N., Wang Y., 2018, *A&A*, preprint ([arXiv:1801.10331](https://arxiv.org/abs/1801.10331))
- Zinchenko I. et al., 2015, *ApJ*, 810, 10

## SUPPORTING INFORMATION

Supplementary data are available at [MNRAS](https://www.mnras.org/) online.

M17\_supp\_material.pdf

Please note: Oxford University Press is not responsible for the content or functionality of any supporting materials supplied by the authors. Any queries (other than missing material) should be directed to the corresponding author for the article.

## APPENDIX A: DETAILS OF THE CLASSIFICATION OF YOUNG STELLAR OBJECTS

Based on IRAC colours or fitting models for the observed SEDs or excess X-ray emission, a number of studies have been made in the literature to identify YSOs in the M17 complex (Povich et al. 2009; Povich & Whitney 2010; Bhavya, Subramaniam & Kuriakose 2013; Broos et al. 2013; Povich et al. 2013, hereafter literature catalogues). For identifying potential YSO candidates in the vicinity of jets/knots, we began our search by using the above

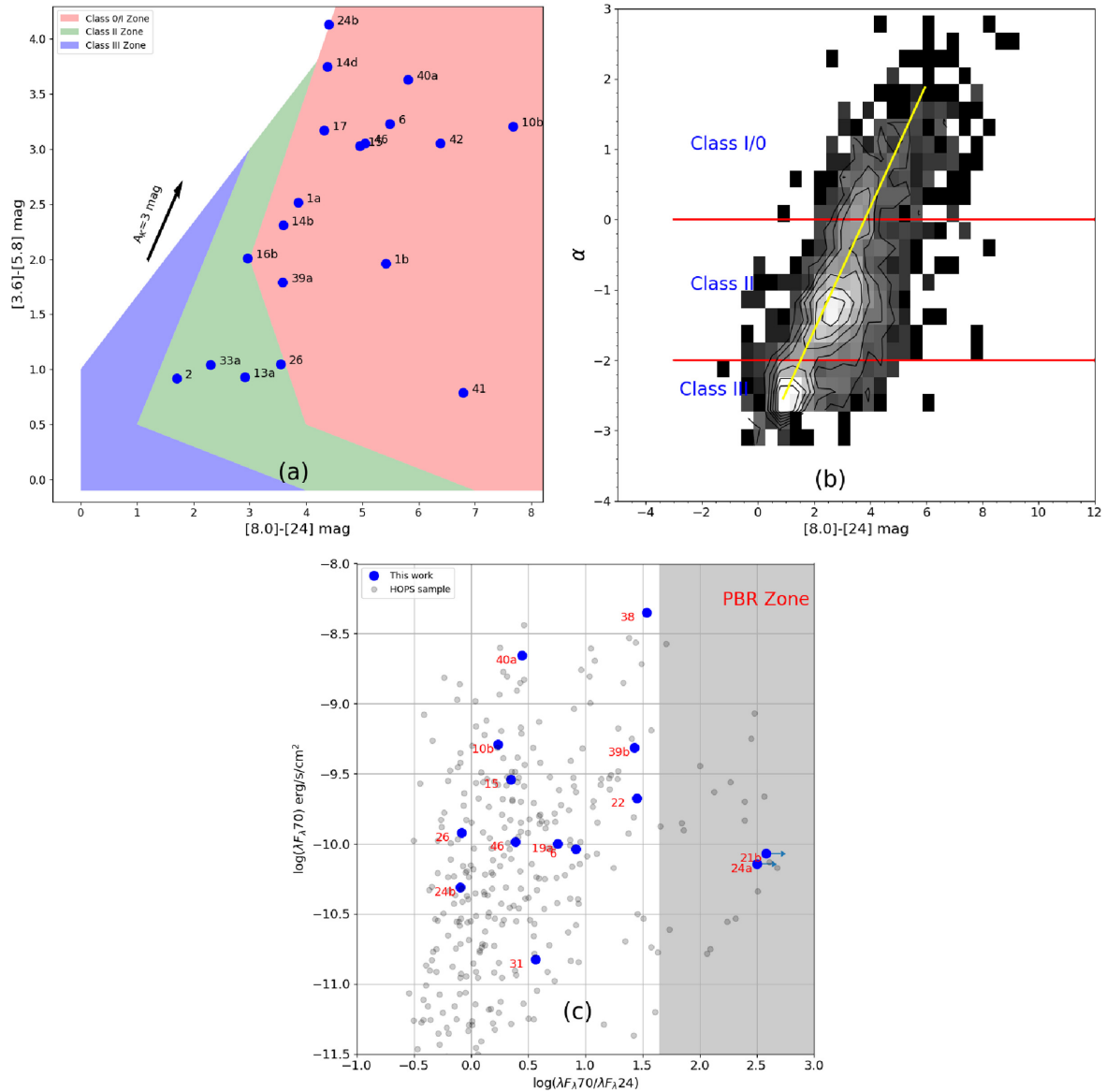


**Figure A1.** Classification of the potential driving sources with different criteria. (a)  $[3.6] - [5.8]$  versus  $[8.0] - [24]$  colour–colour plot of all the potential outflow-driving sources (blue dots). (b) Hess diagram between  $[8] - [24]$  colour and  $\alpha$  of Dunham et al. (2015)’s YSO sample. The yellow line corresponds to the linear fit to the peak of the  $[8] - [24]$  colour distribution, binned in  $\alpha$ . (c)  $70\text{-}\mu\text{m}$  flux versus  $70\text{-}$  to  $24\text{-}\mu\text{m}$  flux ratio for potential outflow-driving candidates (blue dots). Sources without  $24\text{-}\mu\text{m}$  detection are indicated with arrow marks. The shaded area (i.e.  $\log(\lambda F_{\lambda,70})/(\lambda F_{\lambda,24}) > 1.65$ ) represents the zone where early class 0 objects (or PBRs) lie. The protostars from the HOPS sample are shown by grey dots.

literature catalogues; however, these catalogues are incomplete, as none of them has incorporated the  $70\text{-}\mu\text{m}$  data and some of them have not used  $24\text{-}\mu\text{m}$  data. Moreover, we found that many bright  $24\text{-}\mu\text{m}$  sources in the vicinity of jets/knots are visible in only one or two IRAC bands (e.g. see Fig. 3). These sources could be YSOs, but are not listed in the literature, as they failed to pass through the colour combinations or data range used for the YSO identification. Since we are interested only in those sources that are close to jets/knots and, moreover, the number of MHOs in our case is reasonably small, a detailed inspection and classification of point sources around each MHO is possible. Therefore, in addition to the above literature catalogues, we used a set of colour diagnoses between  $3.6$  and  $70\text{-}\mu\text{m}$  (described below) to classify all those potential point sources (e.g. see sources 21a, 21b and 21c in Fig. 3) with possibility of being an outflow-driving source. We particularly paid attention to those

sources that are detected at  $24/70\text{-}\mu\text{m}$  and lie close to jets/knots. For sources that are visible at  $\leq 8\text{-}\mu\text{m}$ , we mostly used literature catalogues to infer their evolutionary status.

The infrared spectral index ( $\alpha$ ), which is the slope of the SED between  $2$  and  $24\text{-}\mu\text{m}$ , is used as an indicator of the YSO evolutionary stage (Lada 1987). In this scheme,  $\alpha > 0$  represents class 0 or I (i.e. rising SED sources with strong spherical envelopes),  $\alpha$  between  $0$  and  $-2$  represents class II (i.e. PMS stars with optically thick accreting discs) and  $\alpha$  between  $-2$  and  $-3$  represents class III (i.e. PMS stars with little or no disc left). Robitaille et al. (2006) introduced the alternative nomenclature ‘stage 0/I, II, III’, equivalent to the above classes but based on the physical properties of YSOs obtained using radiative transfer models. Based on the distribution of young sources of the above classes or stages on the IRAC and MIPS colour–colour diagrams, several colour schemes have been

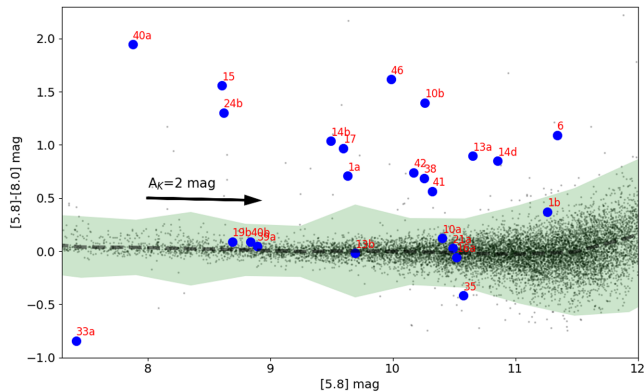


**Figure A2.** [5.8] – [8.0] versus [5.8] colour–magnitude diagram for potential outflow-driving candidates (blue dots) and sources of the field region (black dots). The shaded area represents the  $\pm 3\sigma$  zone around the median [5.8] – [8.0] colour of the field stars.

developed in the literature to classify YSOs (e.g. Allen et al. 2004; Robitaille et al. 2007; Gutermuth et al. 2009; Rebull et al. 2011). However, we note that ambiguity is an inherent property of any YSO taxonomy, whether based upon colours, spectral indices or physical properties, and various schemes can alter classification by 20 to 30 per cent (e.g. Crapsi et al. 2008; Heiderman & Evans 2015; Carney et al. 2016). Keeping this caveat in mind, for simplicity, here we used the term ‘class’ to refer to either the physical stage or observational class of a YSO and adopt the following colour schemes to classify the potential sources into various YSO classes.

(i) For those potential sources that are detected in both IRAC and MIPS bands, we used the [3.6] – [5.8] versus [8.0] – [24] colour–colour scheme (Robitaille et al. 2007) for classification. The distribution of such sources in the [3.6] – [5.8] versus [8.0] – [24] colour–colour space is shown in Fig. A1(a). As can be seen, the majority of these sources are class 0/I-type YSOs. Though high extinction can affect the above classifications, the effect should be minimal in our case. For example, even if we deredden the sources with a foreground extinction of  $A_K \sim 3$  mag (indicated in the figure), most of our candidates will still remain in the zone of class 0/I.

(ii) We observed that a few potential point sources in the vicinity of jets/knots are invisible at 3.6 or 4.5- $\mu\text{m}$ , yet are detected at  $\geq 5.8$ - $\mu\text{m}$  (possibly due to extreme visual extinction), while a few other point sources have no detection in the 5.8- and/or 8.0- $\mu\text{m}$  band (likely due to low sensitivity of these bands) but are detected at  $\geq 24$ - $\mu\text{m}$ . To classify the sources in the former category, we looked for a correlation between [8] – [24] colour and  $\alpha$  using Dunham et al. (2015)’s YSO sample (shown in Fig. A1b). Dunham et al. (2015) compiled spectral energy distributions for 2966 YSOs and tabulated the infrared spectral index, bolometric luminosity and bolometric temperature for each YSO. As can be seen from Fig. A1(b), despite significant scatter, a strong correlation between [8] – [24] colour and  $\alpha$  is clearly evident in the figure. From this correlation, we infer that sources with [8.0] – [24] mag  $> 3.9$  and  $3.9 > [8.0] - [24] \text{ mag} < 1.8$  are, respectively, the class 0/I and class II spectral sources. To classify the sources in the latter category, following the suggestion of Gutermuth et al. (2009), we considered them as class 0/I YSOs if they have [X] – [24] colour  $> 4.5$  mag, where [X] is the photometry in either of the first two IRAC bands.

(iii) We also observed that, in the vicinity of a few MHOs, some of the point sources are either invisible or very faint at 24- $\mu\text{m}$  but significantly bright at 70  $\mu\text{m}$  (e.g. source 21b in Fig. 3). They

could be deeply embedded YSOs of the complex. In such cases, we used the 24- and 70- $\mu\text{m}$  colour combinations for classification. The advantage of using 70- $\mu\text{m}$  is that it is less sensitive to circumstellar extinction and geometry of the disc (Dunham et al. 2006) and is proven as an important wavelength to identify early class 0 sources. For example, based on *Herschel* 70- $\mu\text{m}$  observations, Stutz et al. (2013) identified 18 sources in the Orion complex that are visible at  $\geq 70$ - $\mu\text{m}$ . They named these sources ‘PACS Bright Red sources’ (PBRs). Comparing the SEDs of PBRs with radiative transfer models, they infer that PBRs are very early class 0 objects, when the envelope is massive and the protostar still has to accrete most of its mass. They found that PBRs have very red mid- to far-infrared colours, i.e.  $\log(\lambda F_\lambda 70)/(\lambda F_\lambda 24) \geq 1.65$ . Their analysis also showed that the well-known class 0/I sources of the Orion complex from the *Herschel* Orion Protostar Survey (HOPS) have  $\log(\lambda F_\lambda 70)/(\lambda F_\lambda 24) > 0.0$ . We followed the criteria of Stutz et al. (2013) (shown in Fig. A1c) to understand the evolutionary status of bright 70- $\mu\text{m}$  sources as well as to confirm the classification of the YSOs (i.e. those sources with 70- $\mu\text{m}$  detection) identified in the aforementioned schemes. As can be seen from Fig. A1(c), most of the 70- $\mu\text{m}$  detected sources (blue dots in the figure) have  $\log(\lambda F_\lambda 70)/(\lambda F_\lambda 24)$  greater than 0.0, therefore they are most likely protostars, among which three sources are likely PBRs (one PBR is not shown in the plot, owing to its high  $\log(\lambda F_\lambda 70)/(\lambda F_\lambda 24)$  value).

(iv) For a few MHOs, we observed bright IRAC sources at the centre of bipolar flows with no 24-/70- $\mu\text{m}$  counterparts (e.g. source 21a in Fig. 3). These sources could be low-luminosity class II/III YSOs, so the possibility of missing such YSOs in the aforementioned schemes exists. In such cases, we used literature catalogues, as many of them have used near-infrared and X-ray excess emission characteristics of point sources to classify them as YSOs. It is worth mentioning that X-ray emission is more sensitive to the detection of class III YSOs, while near-infrared excess is more sensitive to the detection of class II YSOs. In addition, we also used the [5.8] versus [5.8] – [8.0] colour–magnitude diagram (CMD) to examine the possibility of such sources as YSOs, because [5.8] – [8.0] colour is an extinction-free indicator, as extinction laws are nearly same at 5.8 and 8.0- $\mu\text{m}$  (e.g.  $A_{5.8}/A_K=0.40$  and  $A_{8.0}/A_K=0.41$ : Weingartner & Draine (2001), see also Chapman et al. (2009)). Thus, in the [5.8] versus [5.8] – [8.0] diagram, infrared-excess sources are expected to appear red in colour, whereas background-reddened sources in the direction of M17 would appear nearly colourless and are likely to fall in the zone of field stars. To see the distribution of field stars in the CMD, we used a field region located  $\sim 1^\circ$  south-east of the H<sub>II</sub> region that is devoid of cold dust emission and has no active site of star formation as per the SIMBAD data base. Fig. A2 shows the distribution of field stars (grey dots) and all potential IRAC sources, including those already identified as YSOs in the aforementioned schemes (blue dots). From Fig. A2, we consider a potential IRAC-only source as a possible YSO if its [5.8] – [8.0] colour is redder than  $3\sigma$  of the median [5.8] – [8.0] colour of the field stars (shown as the blue shaded area) at its corresponding 5.8- $\mu\text{m}$  magnitude. Doing so, we found that most of the potential IRAC-only sources are likely field stars, as most of them are located in the shaded area of the plot and none of them has been identified as a YSO in the literature.

In all the figures, the ID numbers represent the IDs assigned to the MHOs (see Table 1) and the subscripts ‘a’, ‘b’ and ‘c’ of a given ID represent the multiple potential sources of that ID that are under discussion (e.g. see Fig. 3). All the above potential driving sources are marked and discussed in Appendix B, where images of individual MHOs are shown and discussed.

After classifying all the potential sources into various YSO classes as described above, along with catalogues of clumps/cores and other indicators, we looked for the most probable driving sources of MHOs. A summary of our approach is mentioned briefly in Section 4.1 and the details are discussed in Appendix B, where the individual MHOs are discussed. Briefly, we disqualified 12 nearby sources (IDs 1b, 2, 10a, 13b, 16a, 16b, 19b, 21a, 33a, 35, 39a and 40b of Figs A1 and A2) from our driving source list. Among the remaining potential sources, we conclude that 18 outflows are driven by protostars (class 0/I YSOs), 2 are driven by evolved sources (class II YSOs) and 4 are driven by one of the members of a group of YSOs (or small cluster).

## APPENDIX B: MULTIWAVELENGTH IMAGES AND NOTES ON INDIVIDUAL MHOS

Here, we present multiwavelength figures of the region around the MHOs and discussion concerning their morphologies, possible driv-

ing sources, and association with clumps/cores, dark clouds and SiO emission. In all the figures, the images and symbols, respectively, have the same meaning as in Figs 3 and 4, except for the SCUBA cores, which are (if found) shown by diamond symbols. The figures and related discussion are available as supporting information with the online version of the article. We note that the reduced continuum-subtracted H<sub>2</sub> images used in this work are publicly available at <http://astro.kent.ac.uk/uwish2/index.html> and all multi-wavelength figures of the MHOs are available at the MHO data base hosted at <http://astro.kent.ac.uk/~df/MHCat/>.

This paper has been typeset from a  $\text{\TeX/L\AA\TeX}$  file prepared by the author.